Engineering Structures 292 (2023) 116467

Contents lists available at ScienceDirect

Engineering Structures

journal homepage: www.elsevier.com/locate/engstruct

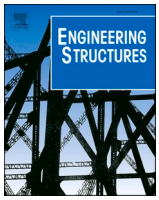

Experimental investigation of bond and crack behaviour of reinforced concrete ties using distributed fibre optical sensing and digital image correlation

Tena Galkovski *, Jaime Mata-Falcón, Walter Kaufmann

Institute of Structural Engineering (IBK), ETH Zürich, Zürich, Switzerland

ARTICLE INFO

Keywords:
Structural concrete
Experimental investigation
Bond behaviour
Crack behaviour
Splitting
Distributed fibre optical measurements
Digital image correlation
Bond stress distribution
Relative rib area

ABSTRACT

The interaction of reinforcing steel and concrete is decisive for the structural behaviour of reinforced concrete (RC) in the serviceability and ultimate limit state. In the past decade, distributed fibre optical sensing (DFOS) and digital image correlation (DIC) have emerged as valuable tools to investigate and comprehend the mechanics of this interaction in more detail. This paper presents and discusses the results of an experimental campaign comprising 21 RC ties subjected to monotonic and cyclic uniaxial tension, where these refined instrumentation methods were utilised to study the influence of the reinforcing bar diameter, rib geometry and mechanical properties on the structural behaviour. Local strains were measured along the reinforcing bars with DFOS, from which the distributions of steel and bond stresses, as well as slip were derived. The crack pattern and kinematics on the surface were determined through DIC. The results allowed studying the influence of the deformation level, cyclic loading and the rib geometry on splitting and the magnitude of local and average bond stresses. The results indicate that the bond and crack behaviour depend on parameters typically neglected in design standards, such as the relative rib area, elastic steel stiffness, and bar diameter. Moreover, the observed average bond stresses in the elastic range were lower than proposed by design standards for serviceability verifications. These observations allow identifying weaknesses and inconsistencies in common bond models, serving as a starting point for improvements in modelling.

1. Introduction

Reinforced concrete (RC) is a composite material where steel bars carry mainly tensile forces and concrete predominantly acts in compression. An adequate interaction between both components is a prerequisite for the structural performance of the composite material, which is highly relevant in the Serviceability Limit State (SLS) by governing the crack behaviour and stiffness of RC, as well as in the Ultimate Limit State (ULS), by influencing the deformation capacity and anchorage of bars. Accordingly, the load transfer between concrete and steel, commonly referred to as bond, has been identified as a critical factor for efficient structural performance from the early beginnings of structural concrete application and research and was investigated thoroughly in the past century.

As acknowledged by the recent state-of-the-art report *fib* Bulletin 72 [1], bond behaviour is highly complex and depends on many parameters including the bar diameter (Ø) and rib geometry as well as the mechanical properties of the reinforcing bars and the concrete, the loading type, the presence of confinement, and the load history. The state-of-the-art on bond in RC established throughout the last century is still subject to uncertainty, as the methods to assess bond were either limited, labour-intensive, or prone to bias the results. Commonly, pull-out specimens were used, and are still standard today [2] to investigate the bond behaviour, determining so-called local bond stress-slip relationships based on global measurements, i.e. (i) the average bond stresses along the embedded length of the reinforcing bar back-calculated from the applied load and (ii) the relative displacement measured at the passive bar end. Extrapolating these bond stress–slip relationships to more complex structures is not straightforward, given the particular conditions in a pull-out test, in which the introduced compressive stress and the embedment length influence the results. Moreover, the bond stresses are far from being uniformly distributed along the embedded length even in pull-out tests with short embedment lengths of merely 5Ø [3]. In order to gain a better understanding of the bond behaviour, researchers used strain gauges glued onto [4] or inside

* Corresponding author.
E-mail addresses: galkovski@ibk.baug.ethz.ch (T. Galkovski), mata-falcon@ibk.baug.ethz.ch (J. Mata-Falcón), kaufmann@ibk.baug.ethz.ch (W. Kaufmann).

https://doi.org/10.1016/j.engstruct.2023.116467
Received 16 February 2023; Received in revised form 9 May 2023; Accepted 9 June 2023
Available online 27 June 2023

Nomenclature

Latin lower case

b	width
f_{cm}	mean concrete cylinder compressive strength
f_{ct}	concrete tensile strength
f_R	relative rib area
f_{su}	steel ultimate stress
f_{sy}	steel yield stress
h_R	rib height
n	modular ratio ($=E_s/E_c$)
s_R	rib spacing
s_r	crack spacing
s_{Rc}	clear rib spacing
u	deformations in x direction
x, y, z	cartesian coordinates

Latin upper case

A_{gt}	steel strains at the ultimate strength
A_R	area of the projection of a single rib
E_c	Elastic Modulus of concrete
E_s	Elastic Modulus of steel
F	force, applied external load
L	length
L_s	the steel reinforcement length
N	cycle number

Special characters

Ø	reinforcing bar diameter

Greek lower case

δ	slip
ε	strains
λ	crack spacing factor according to the TCM
ρ	reinforcement ratio
σ	normal stresses
τ_b	nominal bond shear stresses

Indices

av	average
c	concrete
el	elastic
inf	lower part
lim	limit
m	mean
r	crack
s	steel
sup	upper part
u	ultimate limit state
y	yielding
0	regarding the initial state

[5–7] the bars to determine steel strains from the early 1950s to current times. While these procedures allow measuring bond stresses in different conditions (e.g. lap splices), they may bias the behaviour of the reinforcing steel as well as the interface [8,9], are cost and labour-intensive, and provide only limited, discrete information on steel strains. In addition, these measurements are often not suitable for the experimental investigation of tension chords since the crack locations are typically not known beforehand (natural scatter), and strain minima and maxima are not guaranteed to be captured. While semi-empirical models, typically accounting for the effect of various parameters by modifications to the standard bond stress-slip relationship, were fitted to such data and implemented in design codes, the limited direct experimental insight, combined with the complexity of the behaviour, has obstructed the development of more refined mechanical bond models.

Over the past decade, distributed fibre optical sensing (DFOS) and digital image correlation (DIC) have emerged as valuable tools having the potential to improve the understanding of the mechanics of structural concrete. DFOS has proven particularly useful to study the local bond behaviour [8,9]. This measurement technology allows for quasi-continuously measuring strains up to 3…4% along reinforcing bars instrumented with fibre optical sensors, assessing the strain distribution with a resolution down to 0.65 mm, frequencies above 1 Hz and hardly any interference on the behaviour, as the disturbance of the steel material behaviour is minimal and no ribs have to be removed [8,9]. With the measured strains along the reinforcing bars and the constitutive law of the reinforcing steel, the steel stress profile can be determined, from which the bond stress distribution can be obtained from equilibrium. DFOS has already been successfully applied in the experimental investigation of structural concrete by various authors investigating, e.g. the initial strain and stress state in RC, bond and reinforcement ratio in flexural elements, cyclic loading, splitting, and the influence of the casting direction on bond [8–16], and guidance for the application has been proposed and verified [8,9,15]. These studies have proven that DFOS is an invaluable tool for the experimental research of reinforced concrete and poses an important step forward. The sensing technique could lay the ground for enhanced modelling and leaner design, but its application at a structural level is still scarce.

2. Research significance

The application of distributed fibre optical sensing (DFOS) is relatively new and its use at a structural level is still limited to date. This study exploits the new possibilities offered by DFOS instrumentation to investigate mechanisms of local bond and internal cracking in detail and under more realistic conditions than the commonly used pull-out tests. To this end, an experimental campaign consisting in 21 RC ties loaded in uniaxial tension was carried out, in which the reinforcement strains were measured with DFOS and the crack kinematics were monitored with digital image correlation (DIC). Both technologies combined provide unprecedented insights into the bond behaviour [16], since the detailed internal information provided by DFOS is complemented by the assessment of the cracks at the surface by DIC, and the instrumentation can be applied to complex test setups with realistic boundary conditions. The measurements allow verifying common modelling assumptions for bond in detail, particularly the development of bond stresses as a function of (i) the loading (level of applied load, monotonic or cyclic loading), (ii) the reinforcing bar characteristics (diameter, steel grade and relative rib area) and (iii) the crack development (spacing of main cracks, formation of longitudinal splitting cracks). The data provides a new understanding of local mechanical phenomena in bond, which has been investigated for over a century with limited means of instrumentation, setting a basis for further research in the field.

3. Common modelling assumptions for bond

As mentioned in the introduction, the complex local interaction of concrete and reinforcement is commonly modelled using so-called bond stress-slip relationships, relating nominal bond stresses (shear stresses assumed to be uniformly distributed around the perimeter of the reinforcing bar) to the slip (relative displacement between reinforcing bar and concrete). The nominal bond stresses τ_b in such relationships include forces transferred between concrete and reinforcement by

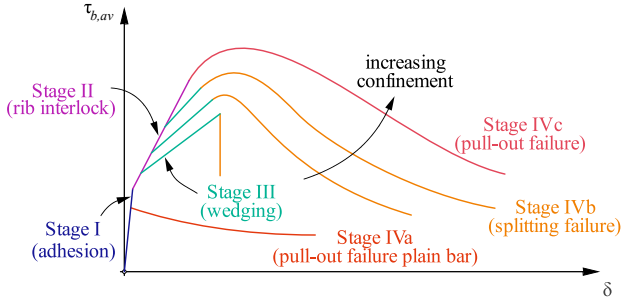

Fig. 1. Stages of bond development defined in the *fib* Bulletin 10 shown on the average bond stress – slip relationship [17].

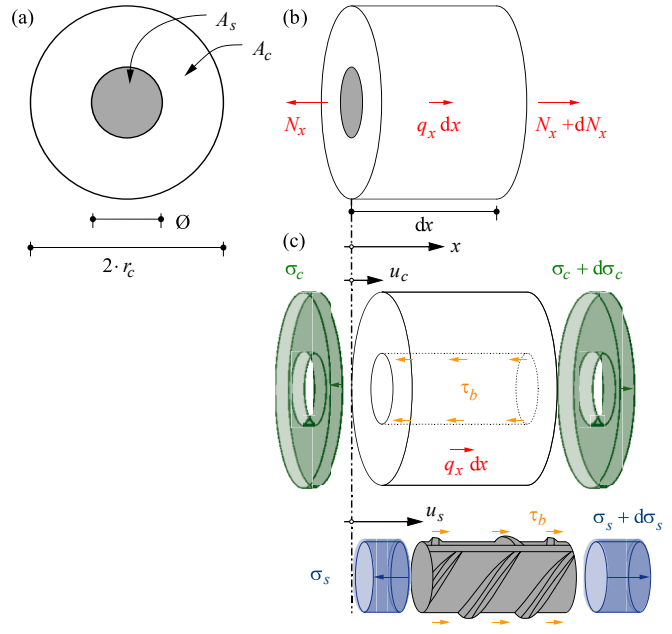

Fig. 2. Differential tension chord element with (a) cross-sectional geometry; (b) general geometry with applied axial loads; and (c) steel, concrete, and bond shear stresses and axial line load acting on the separated steel and concrete elements.

different mechanisms. The commonly recognised stages of local bond development are summarised, e.g. in the *fib* Bulletin 10 [17] (see Fig. 1). Stage I is governed by chemical adhesion ($\tau_b \leqslant \tau_1 = (0.2...0.8)\cdot f_{ct}$) at negligible slip. For plain bars, a pull-out failure would follow immediately (Stage IVa). For deformed bars, Stage II follows, where transverse micro-cracks originate at the tip of the ribs, causing slip and increasing bond stresses by gradually activating the interlock between the reinforcing bar ribs and the concrete keys. In Stage III, the concrete is crushed in front of the ribs, with the crushed concrete causing radial compressive stresses (wedging action) while the bond stresses keep increasing, $\tau_b > (1...3)\cdot f_{ct}$. Longitudinal splitting cracks start forming radially in this range, as tangential tensile (hoop) stresses resist the radial compressive stresses. Depending on the level of confinement, two types of failure may happen in deformed bars: For low and medium levels of confinement, Stage III ends with the through-cracking of the splitting cracks (Stage IVb in Fig. 1); an abrupt loss of bond occurs in bars with low confinement, while some residual bond strength at high slip might be activated in bars with medium confinement (partially shearing off concrete keys). For heavily confined deformed bars a bar pull-out failure occurs, with a residual strength corresponding to shearing off the concrete keys while splitting over the entire section is avoided (Stage IVc in Fig. 1).

Defining the slip δ as the difference of deformations between steel u_s and concrete u_c, assuming a linear elastic behaviour of concrete and reinforcing steel, and formulating equilibrium on an axially loaded tension chord element of infinitesimal length dx (see Fig. 2), Kuuskoski [18] in 1950 derived the second-order differential equation:

$$\frac{d\varepsilon_s}{dx} - \frac{d\varepsilon_c}{dx} = \frac{d^2\delta}{dx^2} = \frac{4\cdot\tau_b}{Ø\cdot E_s} + \frac{Ø\cdot\pi\cdot\tau_b + q_x}{A_c\cdot E_c\cdot(1-\rho)} \tag{1}$$

where the subscripts s and c denote reinforcing steel and concrete, respectively, $Ø$ = bar diameter, τ_b = bond shear stresses, q_x = axial line load, A = cross-sectional area, $\rho = A_s/A_c$ = reinforcement ratio, ε = strains, and E = modulus of elasticity.

Rehm [19] was the first author to publish a local bond stress-slip relationship $\tau_b(\delta)$ and solve the differential equation of bond (Eq. (1)). Depending on the assumed relationship, the complexity of the solution varies significantly, requiring numerical integration in general cases. Rehm already identified two causes of slip for deformed reinforcing bars: through (i) splitting of the concrete caused by wedging action of the reinforcing bar ribs and (ii) local concrete crushing in front of the ribs. He observed in pull-out experiments that the slip was insensitive to the rib flank angle in the range between 40 and 105°. He reasoned that for these angles, the friction was sufficient to prevent relative displacements at the interface, such that the slip could be attributed entirely to concrete crushing in front of the ribs where the crushed concrete formed a cone with a face angle of 30 to 40°, explaining the similar behaviour for the entire range of rib face angles. Similar results were also reported by Lutz and Gergeley [20]. In contrast, Hamad found that increasing the rib flank angle from 30 to 90° slightly enhanced bond strength, while an increase from 60 to 90° resulted in reduced slip and increased stiffness [21]. Rehm [19] proposed to use the relative rib area f_R as a parameter to characterise the interlocking component of bond. While he used the ratio of rib height to rib spacing as an approximation, the following definition [17] is common today

$$f_R = \frac{A_R}{\pi\cdot Ø\cdot s_R} \tag{2}$$

where A_R = area of a single rib projected into the plane perpendicular to the bar axis. This value had already been identified as a relevant parameter affecting bond more than a century ago [22] and several authors since then reported a high relative rib area f_R to influence slip and bond strength beneficially if enough confinement is provided [23–25]. However, most modern design codes merely specify a minimum value of the relative rib area. The *fib* Model Code 2010 which requires $f_R \geq 0.05$ and states that values above 0.14 may develop higher bond stresses, however, without quantifying them. The influence of the relative rib area in elements is experimentally investigated in this study for elements with low confinement in Section 3 and discussed at the end of Section 4.

Tepfers pointed out that the large deformations of the reinforcement reported by Rehm cannot occur without the formation of internal transverse and splitting cracks in the surrounding concrete [26]. A formation of internal cracks was experimentally demonstrated by Goto [27] who injected ink in tested RC ties and thereby revealed the internal secondary crack pattern, with internal conical cracks extending from the rib tips towards the main cracks, being longer the closer they were to the main cracks. Gambarova and Rosati, based on the results of pull-out tests on pre-split specimens [28], concluded that the bar diameter influences the magnitude of the bond stresses, with higher bond strength and stiffness in small-diameter bars. In addition, they observed that the width of the splitting cracks has a detrimental effect on the structural performance in terms of slip and bond strength, being more pronounced for larger bar diameters.

The above discussion and the comments made in the introduction highlight that modelling the complex interaction of concrete and reinforcing bars by nominal bond shear stresses uniformly distributed

Table 1
Specimen configurations in Series 1: diameter and amount of the reinforcement, type of loading with upper and lower bounds for the cyclic loading (F_{sup}, F_{inf}), the number of cycles, and age at testing.

Specimen	Ø [mm]	ρ_s [%]	Loading	F_{inf} [kN]	F_{sup} [kN]	# cycles [-]	Age at testing [d]
Ø14.M.ND#1	14	0.68	monotonic	–	–		25
Ø14.M.ND#2		0.68		–	–		26
Ø20.M.ND#1	20	1.40	monotonic	–	–		39
Ø14.U.ND#1	14	0.68	cyclic - unloading and reloading	0, 0	45, 75	7, 3	40
Ø14.U.ND#2		0.68		0	75	13	41
Ø14.U.ND#3		0.68		0, 0, 0	83, 80, 85	1, 5, 6	41
Ø20.U.ND#1	20	1.40		0, 0	35, 130	7, 10	42
Ø14.R.ND#1	14	0.68	cyclic – reversed loading	−40	70	8	53
Ø14.R.ND#2		0.68		−40	83	8	56
Ø20.R.ND#1	20	1.40		−70, −70	35, 130	7, 5	62
Ø20.R.ND#2		1.40		−70	130	10	45

around the reinforcing bar perimeter is a crude simplification. Bond stress-slip relationships are thus no unique constitutive relationships, which puts the relevance of the differential equation of bond, Eq. (1), in perspective. Furthermore, rather than the local distribution of stresses and strains, the global structural behaviour accounting for tension stiffening is typically relevant in design, i.e. deformations and crack widths. Since these global results are integrals of the strains over a crack element (CE, an element of a tension chord delimited by two adjoining cracks), they can be predicted using appropriate mean values. In particular, assuming bond stresses independent of the slip, the global structural behaviour can be determined from equilibrium without the need to solve the differential equation of bond. These considerations were the starting point for the establishment of the Tension Chord Model (TCM), originally proposed by Marti et al. [29], which uses a stepped, rigid-perfectly plastic bond stress-slip relationship depending only on concrete strength and the steel stress: the nominal bond stresses are set to $2{\cdot}f_{ct}$ and f_{ct} for steel stresses below and above the yield stress, respectively. Similar bond assumptions have been incorporated for the prediction of crack widths in modern design standards [30–32], typically further simplified by assuming average bond stresses, i.e. constant nominal bond shear stresses over the parts of a reinforcing bar with same direction of slip. Current design codes and the TCM neglect the effect of the rib geometry, the bar diameter, the confinement and cyclic loading on the bond stresses. The influence of these factors is investigated in this study based on two series of experiments.

Table 2
Specimen configurations in Series 2: diameter and amount of the reinforcement, type of reinforcing steel, and age at testing.

Specimen	Ø [mm]	ρ_s [%]	Steel type	Age at testing [d]
Ø16.M.ND#1	16	0.89	normal-strength deformed bar	20
Ø16.M.ND#2		0.89		25
Ø16.M.HD#1	16	0.89	high-strength deformed bar	26
Ø16.M.HD#2		0.89		24
Ø16.M.HM-R07#1	17.6 / 16*	0.89	high-strength machined bar	26
Ø16.M.HM-R07#2		0.89		24
Ø16.M.HM-R15#1	19.2 / 16*	0.89		27
Ø16.M.HM-R15#2		0.89		25
Ø16.M.HM-R23#1	20.8 / 16*	0.89		27
Ø16.M.HM-R23#2		0.89		25

4. Experimental campaign

The experimental study consisted of two experimental series on RC ties loaded in uniaxial tension. The geometry of the specimens was kept constant, except for the length that was slightly larger in Series 2. The first series investigated the influence of the reinforcing bar diameter (and reinforcement ratio) and cyclic loading on the bond and crack behaviour using conventional deformed steel reinforcing bars. In the second series, the influence of the rib geometry and steel grade on the bond behaviour in the serviceability limit state was examined. Table 1 provides an overview of the specimen configurations and applied loading.

4.1. Specimens and materials

4.1.1. Specimen configuration

The overview of the eleven specimens of Series 1 is provided in Table 1. The codification of the specimens is composed of four terms: first the diameter is given, followed by the loading type, the reinforcing steel type and a sample count. There were three different loading types in Series 1: (i) monotonic (M), (ii) cyclic loading that always stayed in tension (U), and (iii) reversed cyclic loading, i.e. negative lower bounds of the load F_{inf} (R). More details of the cyclic loading are given in Section 4.2. All specimens of Series 1 were reinforced with a deformed bar of normal strength (codification ND – B500B European steel type) with a diameter of either 14 or 20 mm. The length of these specimens was 1360 mm (concrete) and 2000 mm (reinforcement), respectively, and their width was 150 mm.

Another ten specimens were tested under a monotonically increasing axial load in Series 2 (see Table 2). The reinforcing bar diameter was kept constant at Ø16 mm and three different reinforcement types were used: (i) normal-strength deformed reinforcing bars (ND), (ii) high-strength deformed reinforcing bars (HD) and (iii) high-strength steel rods (HM) with machined ribs, comprising a continuous spiral with a rib flank inclination of 63.43° to the bar axis (i.e. steeper than usual in deformed bars). The machined rib depth was varied to explore three different relative rib areas: (i) 7% (R07), i.e. a typical value for conventional deformed steel bars, (ii) 15% (R15), and (iii) 23% (R23). More details about the rib geometry are provided in Section 4.1.3. The nomenclature of the high-strength machined steel (HM) is followed by a term that defines the relative rib area. The length of the specimens in

Table 3
Concrete properties of both series.

Series	f_c [MPa]	f_{ct} [MPa]	E_c [GPa]
1	36.1	2.94	30.3
2	33.6	3.20	29.1

Table 4
Material and geometrical properties of the reinforcing steel bars.

Series	Steel type	Diameter Ø [mm]	$f_{sy,stat}$ [MPa]	$f_{sy,dyn}$ [MPa]	$f_{su,stat}$ [MPa]	$f_{su,dyn}$ [MPa]	E_s [GPa]	ε_{su} [‰]	A_{gt} [‰]	h_R [mm]	s_R [mm]	s_{Rc} [mm]	f_R [-]
1	B500B	14	494	517	584	621	192.3	111.7	77.6	1.4	6.5	4	–
	B500B	20	483	505	543	581	197.0	96.5	60.1	1.2	12	9	–
2	B500B (ND)	16	515	540	578	611	198.5	68.2	49.2	1	9	6	–
	Top12 (HS)	16	696	721	865	903	168.0	81.4	56.1	1.2	10	6	–
	ETG88 (HM)	16	694	715	853	887	199.6	79.2	70.6	0.8	12	9.2	0.07
	ETG88 (HM)	16	680	698	824	859	198.6	81.8	69.8	1.6	12	8.4	0.15
	ETG88 (HM)	16	657	683	813	863	194.0	67.5	57.3	2.4	12	7.6	0.23

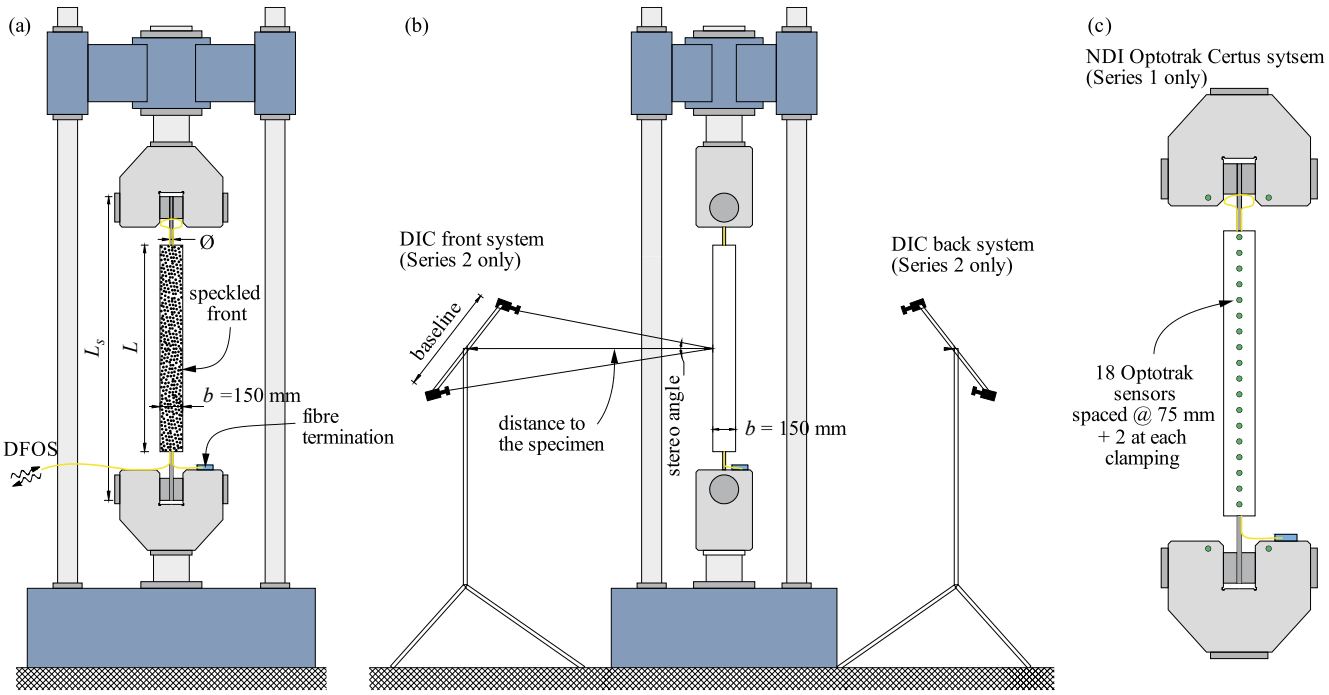

Fig. 3. Experimental setup with an installed specimen in the (a) front view and (b) pseudo-axonometric side view, including the DIC (Series 2 only) and DFOS measurement systems; (c) the Optotrak Certus measuring system from NDI on the specimen back (Series 1 only).

Series 2 was 1500 mm (concrete) or 2100 mm (reinforcement), respectively, and the width remained the same as in Series 1 (150 mm).

4.1.2. Concrete

A concrete with a maximum aggregate size of 16 mm was used in both series. The concrete was delivered from a local ready-mix concrete supplier for each series separately. The secant modulus E_c at 12 MPa and the uniaxial compressive strength f_c were obtained from three standard cylinders with a height of 300 mm and a diameter of 150 mm. The tensile strength f_{ct} was determined from double punch tests [33] on four cylinders with a height and diameter of 150 mm. The mean values of the mechanical properties are summarised in Table 3.

4.1.3. Reinforcing bars

The material properties of the different reinforcing steels were determined on five to six tension tests on bare bars for each grade and are summarised in Table 4; note that while the bars of the HD and HM specimens were corrosion resistant (Top12 commercial name) and produced from special free cutting steel to ease machining (ETG88), respectively, only their mechanical characteristics are relevant here. The static yield and ultimate strength $f_{sy,stat}$ and $f_{su,stat}$ were determined after a 2 min hold allowing for steel relaxation. It can be seen that the machined bars (ETG88 commercial name) had similar mechanical properties as the high-strength deformed bars (Top12), except that the latter exhibited a nonlinear behaviour already at low stresses, causing a lower modulus of elasticity (determined between 100 and 350 MPa). Table 4 also presents some geometrical characteristics including the maximum rib height h_R, the rib spacing s_R, the clear rib spacing s_{Rc}, and the relative rib area f_R. Since the average value of the rib height was not measured, the relative rib area could only be precisely computed for the machined bars, which featured ribs of constant height.

4.2. Test setup and protocol

All tests were performed in the structures laboratory at ETH Zurich using a Schenck universal testing machine. The test setup is illustrated in Fig. 3a and b. The controlled displacement rate of the hydraulic actuator was initially 2 mm/min and was increased up to 7 mm/min in the last part of the plastic range (after $\varepsilon_s \approx 3\%$). Most specimens were loaded monotonically with a uniaxial tensile force to failure. For the other specimens, between one and three sets of cyclic loads were applied, after which they were monotonically loaded in uniaxial tension to failure. Table 1 defines the bounds of the load (F_{inf}, F_{sup}) and the number of cycles for each set of applied cycles. For instance, in Ø14.U.ND#3, an initial load of 83 kN was applied, followed by five cycles between 0 and 80 kN and six cycles between 0 and 85 kN, after which the specimen was loaded until failure (see graphical definition of cycles in Annex A, Fig. 22).

Table 5
Description of fibre optical sensors and devices.

Series	Device	Fibre optical sensor	Coating	Gauge length	Gauge spacing	Measurement frequency
1	ODiSI-A	E9.2/125	Acrylate (mechanical bond)	5 mm	5 mm	1/3 Hz
2	ODiSI-6	SM1250B3(9.8/125)P	Polyimide (chemical bond)	0.65 mm	0.65 mm	6.25 Hz

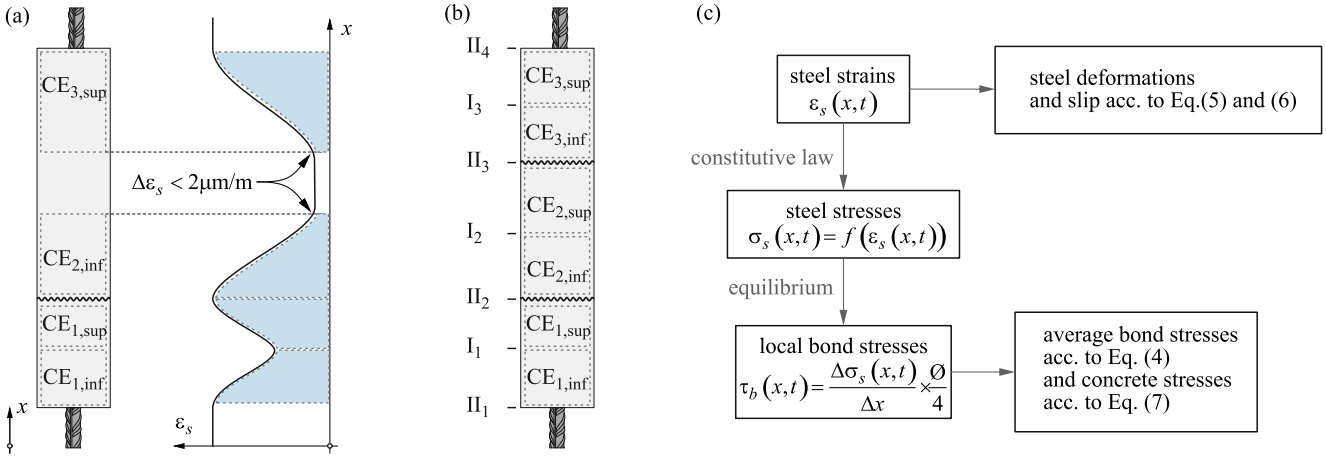

Fig. 4. Derivation of slip and bond stresses from the fibre optical post-processed measurements: division of a tension chord into CE (a) after the first crack and (b) after crack stabilisation; (c) calculation flow chart for a tension chord with *n* CE (Sections I refer to locations where the sign of bond changes, while Sections II refer to cracks and specimen ends).

4.3. Measurement techniques and data evaluation

The applied axial force F_x was measured directly by the load cell of the testing machine. For Series 1, the specimen deformations were measured with the optical 3D motion tracking system Optotrak Certus from NDI. Two sensors of the tracking system were attached at each clamping, and 18 sensors were attached to the back side of each specimen, as shown in Fig. 3c. The mean deformation of the specimen was computed based on the tracked 3D positions of the lowest and highest sensors on the specimen. The crack width was determined based on the relative movement between tracking sensors on both sides of a crack.

The deformations of the RC ties in Series 2 were tracked with DIC (see Section 4.3.1). In all specimens, the reinforcing bar strains were monitored with DFOS (see Section 4.3.2).

4.3.1. Digital image correlation measurements (Series 2)

Two opposite sides of the RC ties of Series 2 were analysed with 3D-DIC, which allowed for measuring the surface deformations of the specimens. Fig. 3b shows the DIC configuration. The equipment on the front side consisted of two FLIR Grasshopper®3 cameras (4096 × 3000 px) with MeVis lenses of 25 mm focal length. The baseline was 1350 mm, the distance to the specimen 3010 mm, and the stereo angle 25.3°, resulting in a resolution of 2.3 px/mm. On the back, two Allied Vision Prosilica GT (6576 × 4384 px) with Zeiss 50 mm lenses were used with a baseline of 1500 mm, a distance of 2430 mm to the specimen and a stereo angle of 34.3°, which leads to a resolution of 3.8 px/mm. A random speckle consisting of black dots of 2.5 mm was applied to both sides. The correlation was performed with the commercial software *VIC-3D* (Correlated Solutions Inc. [34]). The correlation parameters were set to 19 px for the subset size, a step size of 6 px, and a strain filter size of 9. The zero displacement tests (ZDT) performed according to [16] estimated an average noise level of the in-plane displacements $\sigma(U,V)$ around 0.011 mm. The crack kinematics were determined with the open-source software 'Automated Crack Detection and Measurement (ACDM)' [35,36] based on the displacement and strain field measured with DIC.

4.3.2. Distributed fibre optical sensing

4.3.2.1. Equipment configuration. The general procedure for measuring reinforcement strains with DFOS, including the instrumentation of the reinforcing bars, rekeying, and post-processing of the raw data, followed the recommendations of [8]. Prior to casting, two grooves (each 1 × 1 mm) were carved longitudinally in all bars on opposite sides of the cross-section. Subsequently, a glass fibre slightly pre-tensioned to ensure straightness was installed in each groove, fixed with plasticine and magnets, and glued with epoxy. For Series 1, the Optical Distributed Sensor Interrogator ODiSI-A from Luna Innovations Inc. [37] was used in combination with an acrylate-coated single-mode fibre (mode field diameter at 1550 nm of 9.2 μm, cladding diameter 125 μm). For Series 2, the ODiSI-6104 from Luna Innovations Inc. [38] and bend-insensitive, polyimide-coated fibre optical sensors were used (mode field diameter at 1550 nm of 9.8 μm, cladding diameter 125 μm). Further details of the used sensors and spectrometers are summarised in Table 5.

4.3.2.2. Data post-processing. The acquired strains were post-processed to remove local effects caused by ribs and to reduce noise. As a first step, the raw data of Series 2, where very small gauge lengths and spacings had been used at a high sampling frequency, were consolidated to reduce the spatial and temporal resolution: the gauge spacing was increased by a factor of 5 (7 for specimen NS.14-II), and the sampling frequency was reduced to about 1 Hz. Such a data consolidation was not required in Series 1, where the gauge spacing and sampling frequency were set to appropriate values for data acquisition. After removing outliers as in [8] (i.e. values deviating more than three times the standard deviation of the median over a suitable window size), a low pass filter was used in addition to deal with the local disturbances caused by the ribs. The passband frequency of the low pass filter is set to 0.001, the stopband frequency to $0.104/\Delta x$, the passband ripple to 0.01, the stopband attenuation to 20 and the sample rate to $1/\Delta x$, where Δx is the gauge spacing. As a last step, a moving average filter was applied with a window length corresponding to the rib spacing.

The steel stresses, bond stresses (local and average) and the slip were

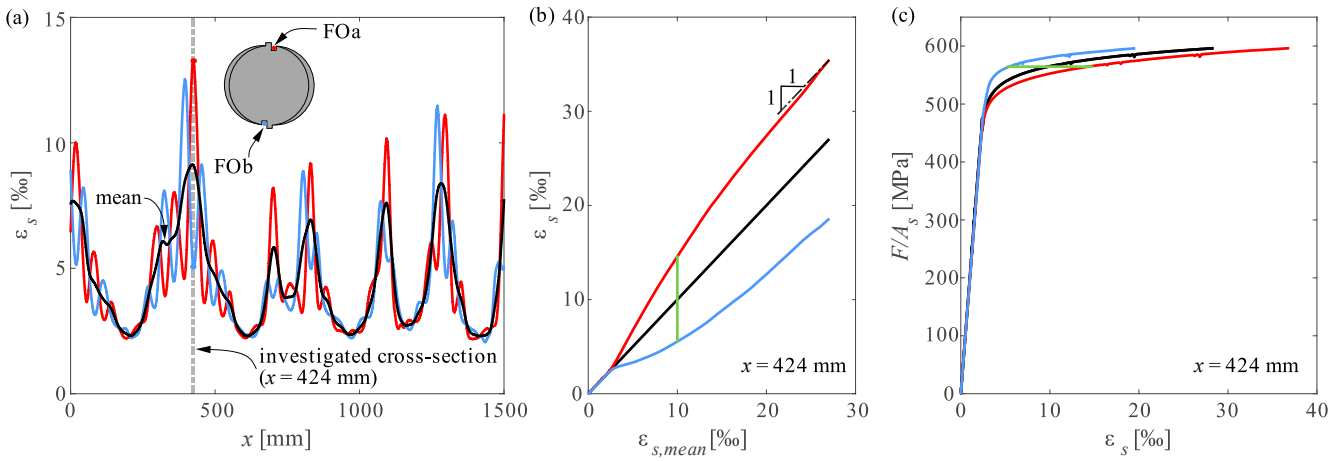

Fig. 5. Irregularities in the deformation measurements of opposite fibre optical sensors for specimen Ø16.M.ND#1 probably due to an axially varying degree of cold-working: (a) strain profile during yielding; (b) local strains against mean local strains at $x = 424$ mm; and (c) mean steel stresses against local and mean steel strains at $x = 424$ mm.

then determined from the post-processed steel strains following the procedure illustrated in Fig. 4. In a first step, the steel stresses σ_s were determined at each data point with the steel strain data and the material constitutive law. For the normal-strength reinforcing bars (B500B) the latter was modelled according to the three-parameter relationship proposed by Ramberg and Osgood in 1943 [39], fitted to the curves of the material tests. For the high-strength steels (Top12), an eighth-order polynomial was used to fit the material characterisation tests since the non-linear elastic behaviour of this steel could not be captured by the Ramberg-Osgood relationship (see Annex B). The DFOS measurements of the machined bars (ETG88) were not evaluated in this study. For unloading and reloading, a linear elastic behaviour with stiffness E_s was assumed for all steel types.

The local bond shear stresses can be determined by formulating equilibrium (see Fig. 2) on a discrete bar element of length Δx defined by two consecutive data points:

$$\tau_b = \frac{\Delta\sigma_s}{\Delta x}\frac{\varnothing}{4} \tag{3}$$

As a next step, average bond stresses can be computed. While determining average bond stresses in pull-out tests is straightforward because the averaging length is known beforehand (embedment length), this is not the case for RC ties because the averaging length is not known beforehand and varies during the test (the point of zero slip cannot be assumed to be at the center between two cracks). Therefore, the following methodology was used to calculate the slip and average bond stresses. In a first step, the tension chord was split into n crack elements (CE) bounded by cracks and specimen ends (referred to as Sections II). Each CE was further subdivided at the locations where the local bond stresses are zero (see Fig. 4a and b), i.e. where the sign of bond changes between two cracks (referred to as Sections I); note that the subscripts "inf" and "sup" denote the lower and upper parts of a CE. The number of CE and the length of the CE parts vary during the crack formation range. This is illustrated in Fig. 4a and b that show the definition of CE for an exemplary tension chord before and after the stabilisation of the crack pattern. Before reaching the fully cracked state, Sections I were defined as the locations closest to a Section II where the variation of the steel strain between consecutive data points did not exceed 2 μm/m, but the numbering of the CE is already based on the fully cracked state. The average bond stress $\tau_{b,av}$ in the lower and upper parts of CE i was then determined as the mean value of local bond stresses over the respective length:

$$\tau_{b,av}\left(\mathrm{CE}_{i,\mathrm{inf}},t\right) = \frac{\int_{x(\mathrm{II}_i)}^{x(\mathrm{I}_i)}\tau_b(x,t)dx}{x(\mathrm{I}_i)-x(\mathrm{II}_i)};\ \tau_{b,av}\left(\mathrm{CE}_{i,\mathrm{sup}},t\right) = \frac{\int_{x(\mathrm{I}_i)}^{x(\mathrm{II}_{i+1})}\tau_b(x,t)dx}{x(\mathrm{II}_{i+1})-x(\mathrm{I}_i)} \tag{4}$$

yielding negative values in the lower parts of the CE where steel stresses diminish in positive direction x. Finally, the slip and concrete stresses can be estimated. The slip is the difference in deformation between steel (u_s) and concrete (u_c):

$$\delta = u_s - u_c \tag{5}$$

The concrete deformations in tension between the cracks were neglected, since they are much smaller than the deformations of the reinforcement. Therefore, the slip was obtained by integrating the reinforcement strains over the distance from Section I (zero slip) in the respective CE to the considered section:

$$\begin{aligned} u_s\left(\mathrm{CE}_{i,\mathrm{inf}},x,t\right) &= \int_{x(\mathrm{I}_i)}^{x}\varepsilon_s(x,t)\mathrm{d}x \quad x(\mathrm{II}_i)\leqslant x\leqslant x(\mathrm{I}_i) \\ u_s\left(\mathrm{CE}_{i,\mathrm{sup}},x,t\right) &= \int_{x(\mathrm{I}_i)}^{x}\varepsilon_s(x,t)\mathrm{d}x \quad x(\mathrm{I}_i)\leqslant x\leqslant x(\mathrm{II}_{i+1}) \end{aligned} \tag{6}$$

Note that for ε_s greater than 0, negative slip (the reinforcing bars is moving downward with respect to the concrete) is correctly obtained for the lower parts of the CE since $x < x(\mathrm{I}_i)$ (integration in the negative direction). Concrete stresses were obtained by integrating the local bond stresses over the distance from the closest Section II (zero concrete stresses) of each CE to the considered section and assumed to be distributed equally over the gross concrete area, i.e.:

$$\begin{aligned} \sigma_c\left(\mathrm{CE}_{i,\mathrm{inf}},x,t\right) &= -\int_{x(\mathrm{II}_i)}^{x}\tau_b(x,t)\cdot\frac{\pi\cdot\varnothing}{A_c}\mathrm{d}x \quad x(\mathrm{II}_i)\leqslant x\leqslant x(\mathrm{I}_i) \\ \sigma_c\left(\mathrm{CE}_{i,\mathrm{sup}},x,t\right) &= -\int_{x(\mathrm{II}_{i+1})}^{x}\tau_b(x,t)\cdot\frac{\pi\cdot\varnothing}{A_c}\mathrm{d}x \quad x(\mathrm{I}_i)\leqslant x\leqslant x(\mathrm{II}_{i+1}) \end{aligned} \tag{7}$$

where the minus sign before the integrals ensures positive concrete stresses over the entire CE since bond stresses are negative (positive) in the lower (upper) parts of the CE while integration is in the positive (negative) direction.

4.3.2.3. Influence of initial strains on the measurement reliability. The bars of Specimens Ø16.M.ND#1 and #2 came from a batch revealing a non-homogeneous initial strain state, similarly as observed by [8]. Fig. 5a shows the strain profiles in Test Ø16.M.ND#1 measured with both sensors(FOa in red and FOb in blue) and their mean value in black. Distinct discrepancies between the results of both sensors with a

Table 6
General results of the test series: initial strains, concrete stress at first cracking, crack spacing, mean strains and mean crack widths.

Series	Specimen	Age at testing	ε_{s0}	$\sigma_{ct,cr}/f_{ct}$	Crack spacing [mm]			Mean strain ε_{sm} [‰] for stresses at the crack σ_s:			Mean crack width w_{cr} [mm] for stresses at the crack σ_s:		
		[d]	[10^{-6}]	[–]	s_{rm}	$s_{r,\min}$	$s_{r,\max}$	300 MPa	500 MPa	σ_{su}	300 MPa	500 MPa	σ_{su}
1	Ø14.M.ND#1	25	−96	0.77	344	298	415	0.03	2.17	25.73	–	1.0	11.6
	Ø14.M.ND#2	26	−108	0.80	447	425	470	0.04	2.73	29.14	–	1.9	20.3
	Ø14.U.ND#1	40	−111	0.70	336	215	423	0.04	1.13	27.18	–	0.5	9.2
	Ø14.U.ND#2	41	−111	0.85	453	360	540	0.11	3.15	38.26	–	1.7	14.2
	Ø14.U.ND#3	41	−75	0.63	458	383	508	0.66	2.61	34.02	0.8	1.9	15.4
	Ø14.R.ND#1	53	−136	0.63	456	363	505	1.23	3.00	37.90	0.9	2.2	26.6
	Ø14.R.ND#2	56	−129	0.61	338	255	483	–	–	–	–	–	–
	Ø20.M.ND#1	39	−97	0.59	337	293	415	0.85	2.36	22.16	0.4	0.5	4.3
	Ø20.U.ND#1	42	–	0.52	269	195	393	1.18	2.31	28.46	0.5	0.8	9.9
	Ø20.R.ND#1	62	−113	0.59	328	205	418	0.94	2.17	20.50	0.4	0.8	4.7
	Ø20.R.ND#2	45	−102	0.51	264	215	345	0.80	2.28	21.66	0.6	0.8	7.4
2	Ø16.M.ND#1	20	−194	0.51	250	124	414	0.89	2.18	25.69	0.3	0.6	6.4
	Ø16.M.ND#2	25	−236	0.51	244	169	315	0.43	1.13	24.71	0.3	0.6	7.0
	Ø16.M.HD#1	26	−241	0.44	375	284	504	0.70	2.12	29.83	0.4	0.8	8.7
	Ø16.M.HD#2	24	−227	0.52	300	227	415	1.04	2.28	33.83	0.4	1.0	12.4
	Ø16.M.HM-R07#1	26	−222	0.46	375	339	430	0.85	1.72	37.90	0.4	0.9	12.8
	Ø16.M.HM-R07#2	24	−233	0.40	375	277	509	0.95	2.00	39.18	0.3	0.6	8.6
	Ø16.M.HM-R15#1	27	−197	0.41	375	233	535	0.94	2.11	38.59	0.4	0.7	9.7
	Ø16.M.HM-R15#2	25	−208	0.37	300	205	486	1.35	2.56	32.84	0.5	0.6	6.4
	Ø16.M.HM-R23#1	27	−189	0.42	250	161	332	1.44	2.67	29.42	0.5	0.7	6.5
	Ø16.M.HM-R23#2	25	−236	0.40	214	124	322	1.04	2.02	34.19	0.2	0.4	6.3

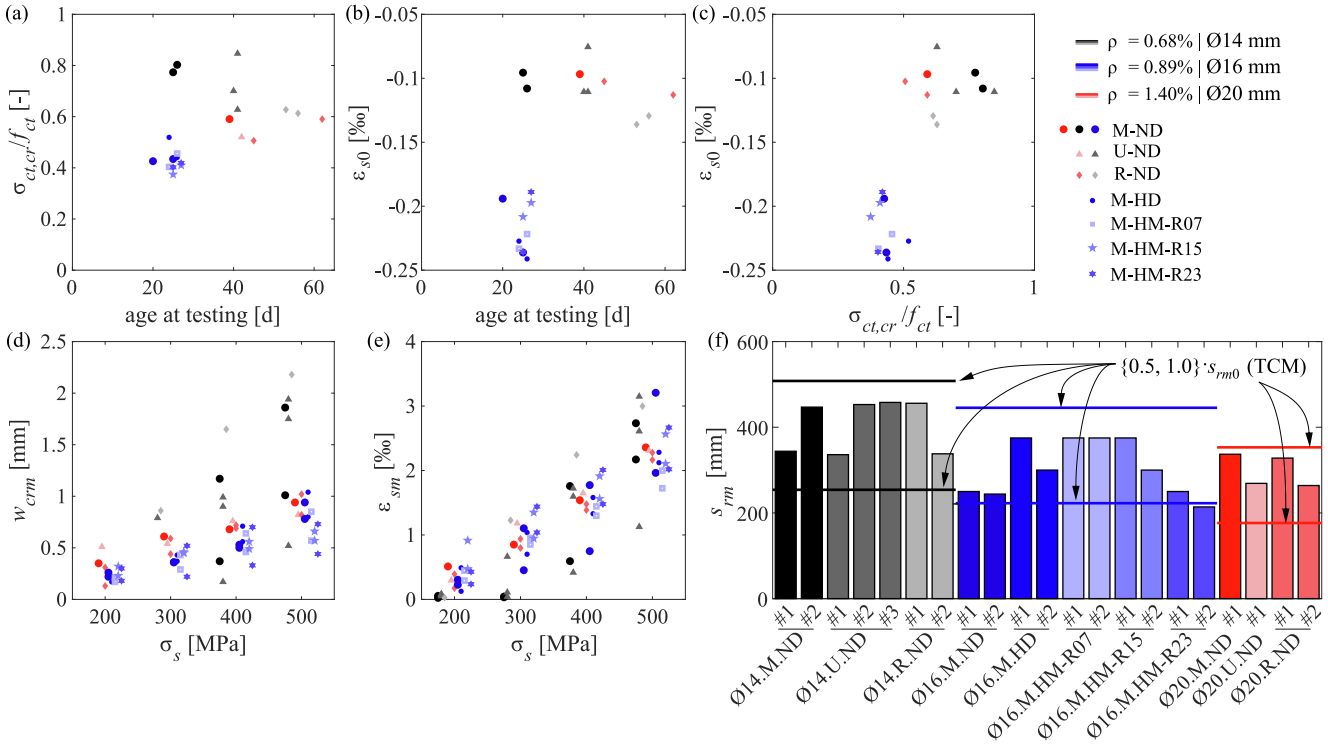

Fig. 6. General results of the experimental campaign sorted by reinforcement ratio ρ, steel type, and loading mode: (a) ratio of effective concrete tensile stress at cracking $\sigma_{ct,cr}$ to tensile strength f_{ct} against testing age; (b) average initial steel strains ε_{s0} against testing age; (c) $\sigma_{ct,cr}$ against ε_{s0}; (d) average crack widths (main cracks); (e) mean tension chord strains; (f) measured average crack spacing, as well as maximum crack spacing (s_{rm0}) and minimum crack spacing ($0.5 \cdot s_{rm0}$) predicted by the Tension Chord Model (TCM) [29].

periodicity of 55 mm are visible in the plastic range. The disparities grow with increasing deformations, as shown in Fig. 5b, where the local strains of both fibres and their average value at $x = 424$ mm are plotted against the average strain $\varepsilon_{s,mean}$ of both sensors. It can be observed that the differences tend to stabilise after large plastic deformations have occurred (the slopes of the red and blue curves tend to be similar), indicating a more uniform deformation behaviour in this range. These differences are presumably caused by the cold-working process leading to different initial strains (and consequently different constitutive behaviour) along the reinforcing bar axis and over the cross-section. Fig. 5c shows the mean stress-local strain relationships. Based on the findings in [8], the average of FOa and FOb can be regarded as reliable, but it highlights the necessity of instrumenting bars with at least two optical sensors.

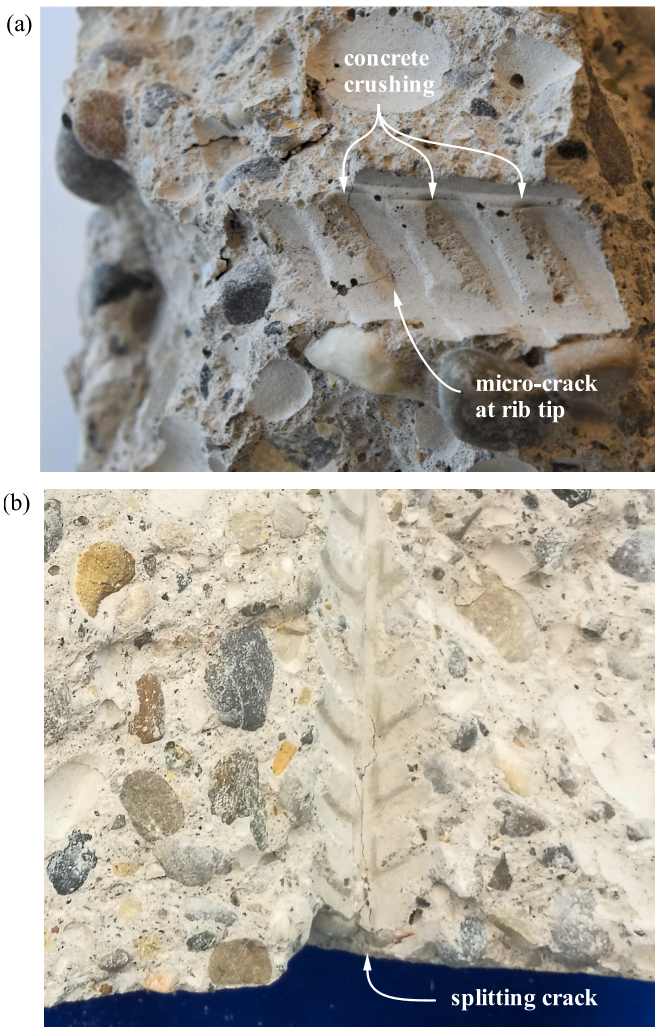

Fig. 7. Internal inspection of selected specimens after testing: (a) concrete crushing at the ribs, micro-crack originating at the first rib from left; (b) splitting of specimen Ø20.M.ND#1.

5. Test results and discussion

5.1. General observations

This section discusses general results about the crack and load-deformation behaviour. Detailed analyses of the bond behaviour are presented in the following sections, starting with general observations about local (Section 5.2) and nominal bond stresses (Section 5.3), followed by an investigation of three selected aspects: splitting (Section 5.4), cyclic loading (Section 5.5) and rib geometry (Section 5.6).

The response of the RC ties was characterised by an initially uncracked range, followed by a crack formation range. After stabilised cracking, the crack width increased quasi-linearly with the applied load until yielding occurred at the cracks. The specimens with Ø20 bars split during the elastic range, while all specimens with Ø16 and some with Ø12 split after steel yielding. During the plastic stage, the yielding of the reinforcement progressed and eventually extended over the entire length of the specimen. The specimens failed in all cases due to steel rupture. In the instance of steel rupture, the concrete of all specimens made of machined bars (HM) split and spalled off entirely. Possible explanations for this behaviour are the high amount of energy stored in the specimens due to the steeply inclined ribs or that the steep, rather sharp ribs caused major internal cracking that severely disintegrated the surrounding concrete, causing the concrete to spall with the dynamic effects at bar rupture.

Table 6 gives an overview of the crack and load-deformation behaviour of both test series. The initial steel strains caused by restraint shrinkage ε_{s0} were measured by DFOS by using the state before concrete casting as reference (mean value over the entire tension chord), while the concrete stresses at first cracking $\sigma_{ct,cr}$ were determined based on the cracking load F_{cr} assuming deformation compatibility over the cross-section:

$$\sigma_{ct,cr} = \frac{F_{cr}/A_s}{1/\rho_s + n - 1} = f_{ct} - \sigma_{c0} \tag{8}$$

where $n = E_c/E_s$ = modular ratio and σ_{c0} = initial concrete stresses. The remaining values in Table 6 (mean s_{rm}, minimum $s_{r,\min}$, and maximum crack spacing $s_{r,\max}$, and mean strains ε_{sm} and crack widths w_{cr} at selected maximum steel stresses) were determined based on the NDI (Series 1) and DIC (Series 2) measurements.

Initial tensile concrete stresses are caused by material inhomogeneity, eccentricities and the restraint provided by the reinforcing bars to the concrete contraction due to hydration heat and shrinkage. The latter can be determined by formulating equilibrium on a section of the tension chord assuming linear elastic behaviour and strain compatibility as [40]:

$$\sigma_{c0} = -E_c \cdot \varepsilon_{cs} \cdot \frac{n \cdot \rho_s}{1 + \rho_s \cdot (n-1)} \tag{9}$$

with ε_{cs} = free shrinkage strain, and are accompanied by initial steel stresses $\sigma_{s0} = \sigma_{c0} \cdot (1\text{-}\rho_s)/\ \rho_s$ and corresponding initial steel strains $\varepsilon_{s0} = \sigma_{s0}/E_s$. As the latter are measured with DFOS, the initial steel and concrete stresses can also be determined experimentally if a homogeneous material behaviour is assumed. Consideration of these initial stresses and strains is essential in studying the behaviour of RC elements in the SLS [9].

While Eq. (9) merely provides a rough estimation due to the large scatter of shrinkage and the further effects causing initial stresses, it indicates that the cracking load may be significantly reduced by initial stresses, and diminishes with increasing shrinkage (i.e. age of testing) and reinforcement ratio while the initial compressive steel stresses and strains increase. Indeed, the experimental results confirm these tendencies, see Table 6 and Fig. 6a and b: With the age of the specimens at testing, the initial compressive steel strains increased and the cracking load decreased (compare, e.g. specimens with ρ_s = 0.68%), and for specimens made of the same concrete, the initial steel strains were smaller at higher reinforcement ratios: The ρ_s = 1.40% samples had smaller concrete tensile stresses at cracking than the ρ_s = 0.68% samples, and smaller initial steel strains. However, the observed cracking loads, in the range of 40…80% of the material tensile strength, are lower than expected when back-calculating them using Eq. (9) and expected shrinkage strains, underlining that predictions of the first cracking load are subject to considerable uncertainty. Comparing the initial steel strains directly to the normalised cracking stress, a correlation between the two can be observed (Fig. 6c).

The mean crack widths and strains compiled in Table 6 are visualised in Fig. 6d and e. The samples with the lowest reinforcement amount (Series 1 with Ø14, ρ_s = 0.68%) exhibited the highest mean strains (once they cracked), and the largest crack widths. The remaining samples had comparable mean strains, but the samples with ρ_s = 1.40% (Series 1, Ø20) had larger crack widths than the samples with ρ_s = 0.89% (Series 2, Ø16). The mean crack spacings (illustrated in Fig. 6f) were within limits predicted by the TCM (i.e. between 0.5 and 1.0 times the theoretical maximum crack spacing s_{r0}) except for specimen Ø16.M.HM-R23#2, which had a very high relative rib area. The mean crack spacing decreased about 43% with increasing relative rib area from HM.07 to HM.23. A more detailed analysis on the influence of the rib geometry on the bond behaviour, which is currently not considered by design codes and neglected by most bond models, is given in Section 5.6.

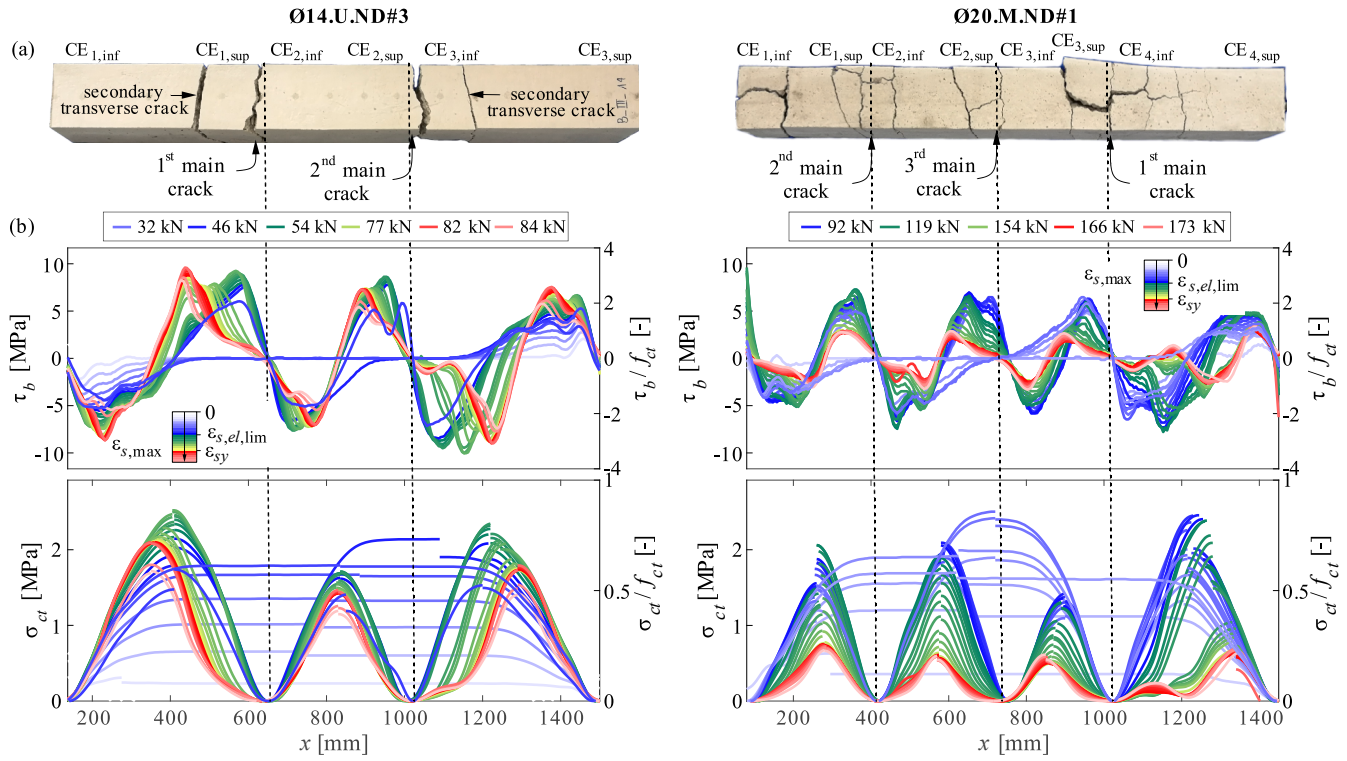

Fig. 8. Bond and concrete tensile stresses for two different bar diameters: (a) crack pattern after failure in which the transverse cracks not marked as main cracks correspond to secondary cracks induced by splitting; (b) development of local bond and concrete tensile stress distribution with increasing loading (blue: linear elastic, green: nonlinear elastic, and red: plastic steel at the crack). (For interpretation of the references to colour in this figure legend, the reader is referred to the web version of this article.)

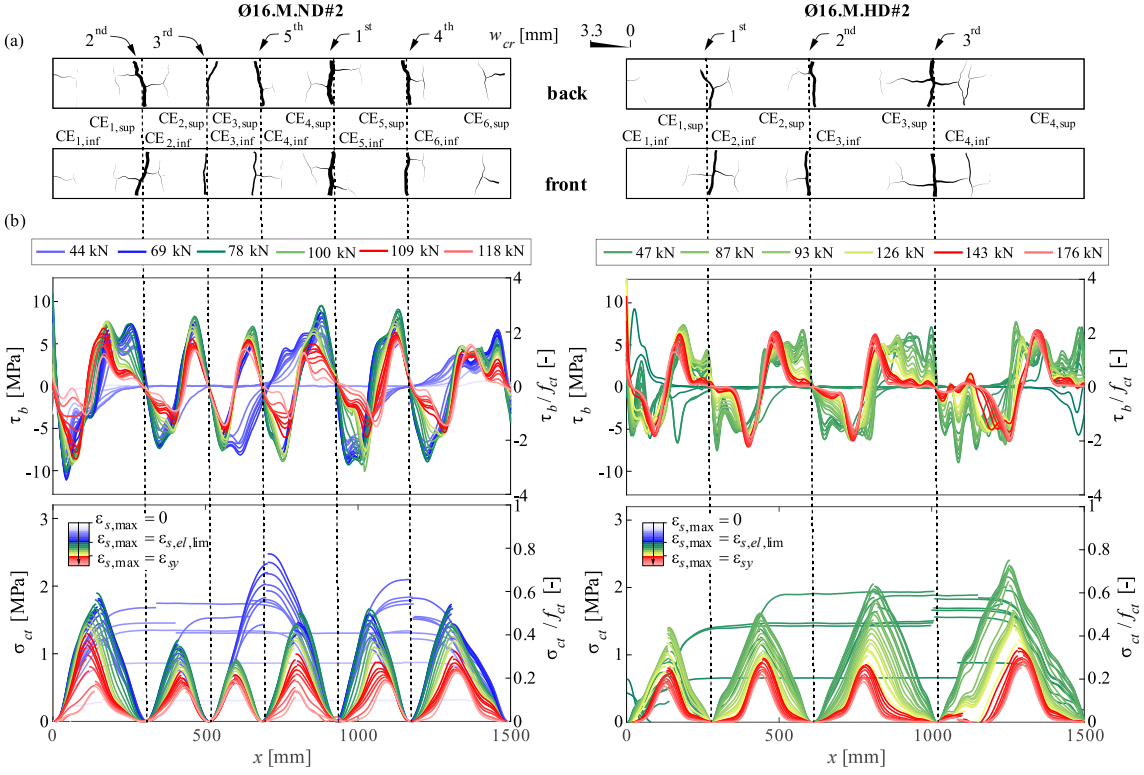

Fig. 9. Bond and tensile concrete stresses for two different steel types of same bar diameter: (a) cracks at $F = 109$ kN (ND) and 143 kN (HD); (b) development of local bond and concrete tensile stress distribution with increasing loading (blue: linear elastic, green: nonlinear elastic, and red: plastic steel at the crack). (For interpretation of the references to colour in this figure legend, the reader is referred to the web version of this article.)

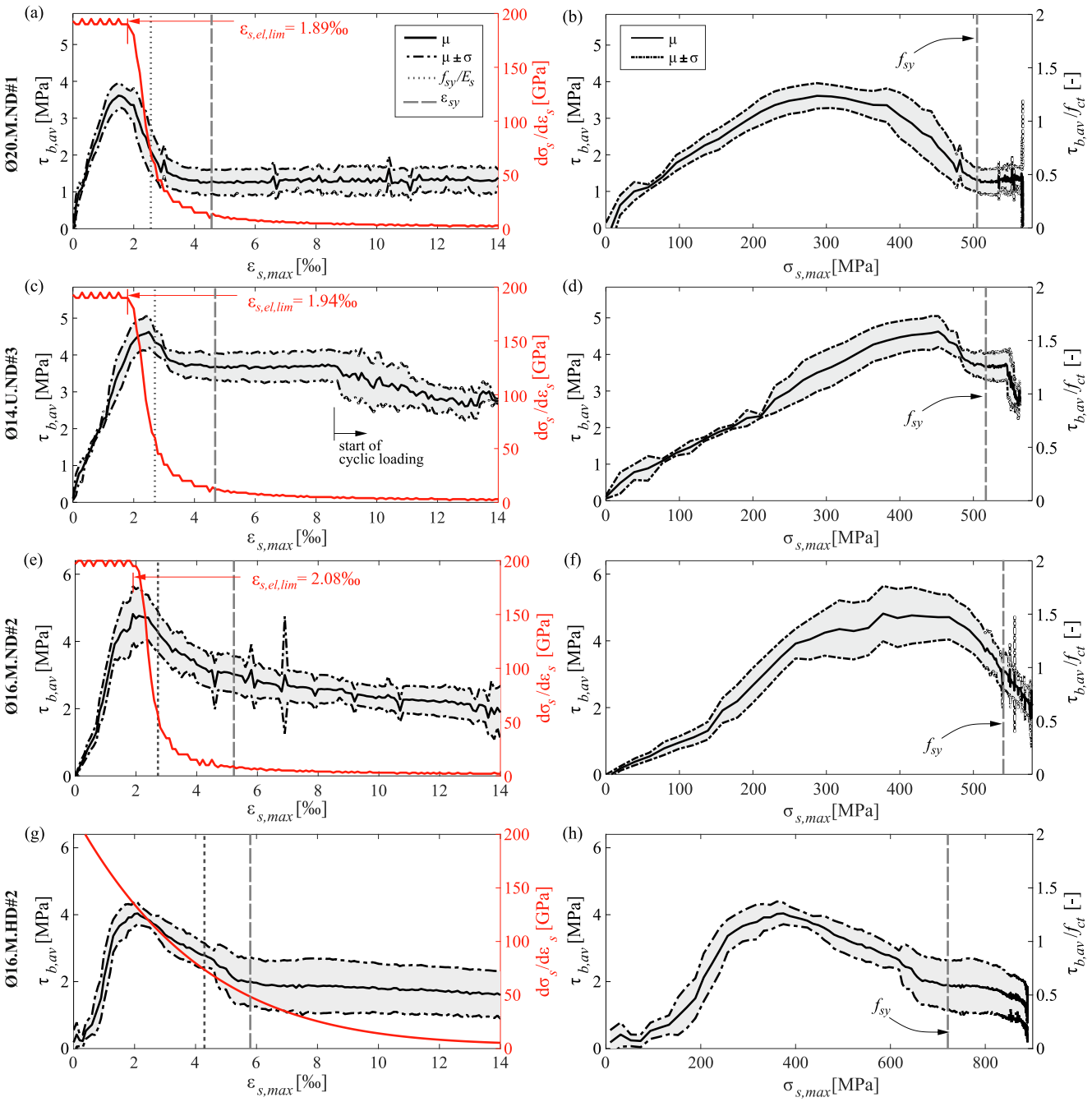

Fig. 10. Mean value μ and standard deviation σ of the average bond stresses over all CE plotted against the maximum steel strain (left) and maximum steel stress (right), for Specimens (a)-(b) Ø20.M.ND#1; (c)-(d) Ø14.U.ND#3, (e)-(f) Ø16.M.ND#2; (g)-(h) Ø16.M.HD#2, with the tangent stiffness of the steel at the crack plotted in red in the left diagrams. (For interpretation of the references to colour in this figure legend, the reader is referred to the web version of this article.)

The reversed loading ($F_{inf} < 0$ kN) and the un- and reloading ($F_{inf} \geq 0$ kN) had no clear influence neither on the load-deformation behaviour nor on the crack behaviour. Its effect on the bond behaviour is studied in detail in Section 5.5.

The specimens and debris were visually inspected after testing to better understand local effects influencing the bond behaviour. Fig. 7 shows two photos of the concrete interface with the reinforcing bar imprint. On the split-off piece in Fig. 7a, concrete crushing occurred in front of the ribs, as observed by numerous authors [17,19,28]. Here, concrete crushing was rarely observed and only near the cracks where the slip was high. A micro-crack that originated from the rib tip can also be seen in Fig. 7a; such micro-cracks in the inspected specimens were much less prominent than reported by Goto [27]. Fig. 7b shows a specimen with splitting failure. The marked splitting crack originated at the interface with the bar but did not reach the concrete surface. This observation implies that splitting starts internally and propagates to the concrete surface. The formation of splitting cracks and its influence on the bond behaviour will be discussed in Section 5.4.

5.2. Local distribution of bond stresses between two cracks

The local distribution of bond stresses is analysed in the following for selected specimens to verify some paradigms discussed in Section 3. The dependency on the load level, reinforcement strength and bar diameter is discussed based on the analysis of the following specimens: Ø20.M.ND#1, Ø14.U.ND#3, Ø16.M.ND#2, and Ø16.M.HD#2.

Table 7
Concrete tensile stresses in cross-sections that were about to crack in chronological order for specimens Ø14.U.ND#3, Ø20.M.ND#1, Ø16.M.ND#2, and Ø16.M.HD#2. The tensile stresses are determined through the integration of bond stresses.

Specimen	Ø14.U.ND#3 (Series 1)		Ø20.M.ND#1 (Series 1)			Ø16.M.ND#2 (Series 2)					Ø16.M.HD#2 (Series 2)		
Crack #	1	2	1	2	3	1	2	3	4	5	1	2	3
$\sigma_{ct,cr} / f_{ct}$	0.62	0.64	0.55	0.64	0.85	0.41	0.55	0.48	0.66	0.77	0.44	0.60	0.59

First, two specimens that differ in bar diameter, reinforcement ratio and relative rib area are compared. Fig. 8a shows the crack pattern of Ø14.U.ND#3 (left) and Ø20.M.ND#1 (right) after testing, and Fig. 8b the local bond stresses and the resulting concrete stresses for different load steps (Ø14.U.ND#3 only before cyclic loading, see Fig. 22a). The lines are blue for maximum strains smaller than the linear limit $\varepsilon_{s,el,lim}$, green between $\varepsilon_{s,el,lim}$ and the yield strain ε_{sy}, and red for higher maximum strains. The linear limit $\varepsilon_{s,el,lim}$ is defined as the strain at which the tangent stiffness of the steel starts to decrease (see the red curves in Fig. 10 for the definition of $\varepsilon_{s,el,lim}$).

During the linear elastic stage, the inclination $d\tau_b/dx$ close to the cracks remained relatively constant, while with increasing loading the peak bond stress rose and moved away from the crack. In the nonlinear elastic range, the inclination decreased either gradually (in the CE not showing splitting) or abruptly (wherever splitting took place). The crack element parts $CE_{1,sup}$ and $CE_{3,inf}$ of Specimen Ø14.U.ND#3 and all of Ø20.M.ND#1, except $CE_{3,inf}$ and $CE_{4,sup}$, exhibited a splitting failure. After splitting, the peak of bond stresses moved visibly away from the cracks.

The peak bond shear stresses for the Ø14 bar ($\sim 3.4 \cdot f_{ct}$) were 75% higher than for the Ø20 bar ($\sim 2 \cdot f_{ct}$), which could be attributed to the smaller bar diameter or – according to current standards ignoring the effect of the bar diameter on bond stresses – the higher relative rib area. The maximum concrete tensile stresses reached about $0.8 \cdot f_{ct}$ in both cases for those CE with large crack spacings. The crack element parts of Ø14.U.ND#3 that split had higher peak bond stresses even after splitting than the ones that did not split. This observation is not in line with the local bond development of the *fib* Bulletin 10 [17], where the bond stresses of a split element are predicted to be smaller.

Fig. 9 shows the local bond stresses observed in two specimen with a normal-strength and a high-strength reinforcing bar of equal diameter (Ø16), with very similar relative rib area and made of the same concrete, Ø16.M.ND#2 and Ø16.M.HD#2. Most CE had splitting cracks, manifesting in a loss of bond over the splitting crack length and a shift of the bond stress peak towards the inside of the CE. Splitting is discussed in more detail in Section 5.4. The HD sample, with the nonlinear stress–strain relationship already at low stresses as described in Section 4.3.2.2, exhibited a fairly uniform distribution of bond stresses and almost linearly varying concrete (and steel) stresses in the serviceability range, differing from the behaviour observed in all specimens with normal-strength reinforcement, which in SLS showed a distinct bond stress peak and hence, a more S-shaped concrete stress distribution. In the two specimens illustrated in Fig. 9, the maximum concrete tensile stresses correlated well with the crack spacing, reaching values up to $0.8 \cdot f_{ct}$ in the longest CE. Although both specimens had identical geometries, Specimen Ø16.M.ND#2 exhibited five and Ø16.M.HD#2 only three cracks. Moreover, after the formation of all cracks (green curves), Specimen Ø16.M.HD#2 exhibited even higher concrete tensile stresses than Ø16.M.ND#2: Cross-sections with concrete tensile stresses larger than $0.6 \cdot f_{ct}$ cracked in Ø16.M.ND#2, but not in Ø16.M.HD#2. Ø16.M.HD#2 had a more uniform bond stress distribution and lower peak values. The different crack spacings seem thus mainly related to initial stresses, inhomogeneity of the specimens and the randomness of crack formation. It should be noted that even in a perfectly homogeneous tension chord there is an uncertainty of a factor of 2 for the crack spacing [29].

Table 7 compiles the concrete tensile stresses transferred to the cross-sections of the cracks by bond immediately before crack formation ($\sigma_{ct,cr}$) for the four specimens shown in Fig. 8 and Fig. 9, obtained by integrating bond shear stresses using Eq. (7). They ranged from 0.55…$0.85 \cdot f_{ct}$ in Series 1, and from 0.44…$0.60 \cdot f_{ct}$ (HD) and 0.41…$0.77 \cdot f_{ct}$ (ND) in Series 2. In almost all cases, $\sigma_{ct,cr}$ increased between the first and the last crack, which might be attributed to material inhomogeneity and secondary bending effects. Even last cracks developed at concrete tensile stresses clearly below the material strength (0.59…$0.85 \cdot f_{ct}$), which can be explained by the initial stresses present at the beginning of the tests (Section 5.1). Presumably for the same reason, the first cracking stresses determined with DFOS (Table 7) differ from those determined through the applied force (Table 6). This applies e.g. to Specimen Ø16.M.HD#2, in which cracking occurred at a location with a stress determined from DFOS measurements of only $0.44 \cdot f_{ct}$, while the stress based on the applied load was considerably higher ($0.52 \cdot f_{ct}$); a similar stress was obtained in the cross-section with the highest concrete stresses ($0.53 \cdot f_{ct}$).

5.3. Average bond stresses

Using average bond stresses in design is preferable to the tedious and computationally inefficient integration of local bond stresses, provided that they realistically represent the structural behaviour. While average bond stresses can be obtained with conventional instrumentation, special test setups such as pull-out tests are required whose extrapolation to more complex structures is not straightforward, as discussed in Section 1.

Alternatively, average bond stresses can be obtained from local bond stress measurements by integration, following the procedures outlined in Section 4.3.2.2 (see Eq. (4)). While until recently, measuring local bond stresses was cumbersome and often biasing the results, such measurements are readily possible using DFOS, allowing to obtain average bond stresses in structural elements. This is illustrated in the following for the specimens from the previous section, and the DFOS results are compared to values commonly used in design.

Fig. 10 presents the mean value μ and standard deviation σ of the average bond stresses of all CE, plotted against the maximum steel strain (left) or maximum steel stress (right), respectively. In the left column, the tangent stiffness of the reinforcing bar steel (from the constitutive law) is plotted against the steel strain, using the right ordinate. The linear limit strain $\varepsilon_{s,el,lim}$ (see Section 5.2) is indicated as well. It can be observed that the peak of average bond stresses was always reached at around 2‰ maximum steel strain. This coincides with the moment when the tangent stiffness of the normal-strength steel starts decreasing ($\varepsilon_{s,el,lim}$). Beyond this value, bond stresses decrease, irrespective of whether splitting was observed or not.

Further, the maximum average bond stresses of the specimens with normal-strength steel bars were found to decrease with increasing bar diameter, from $1.58 \cdot f_{ct}$ for specimen Ø14.U.ND#3 (Ø14 mm) to $1.50 \cdot f_{ct}$ for Ø16.M.ND#2 (Ø16 mm), and $1.27 \cdot f_{ct}$ for Ø20.M.ND#1 (Ø20 mm). The peak average bond stress in the specimen with high-strength reinforcement ($1.26 \cdot f_{ct}$ in Ø16.M.HD#2) was 16% lower than in the specimen with identical properties but with normal-strength reinforcement (Ø16.M.ND#2). The average bond stress of the specimen with high-strength reinforcement also reached its peak at around 2‰ despite having a much higher yield strain. It decreased already by 50% when the

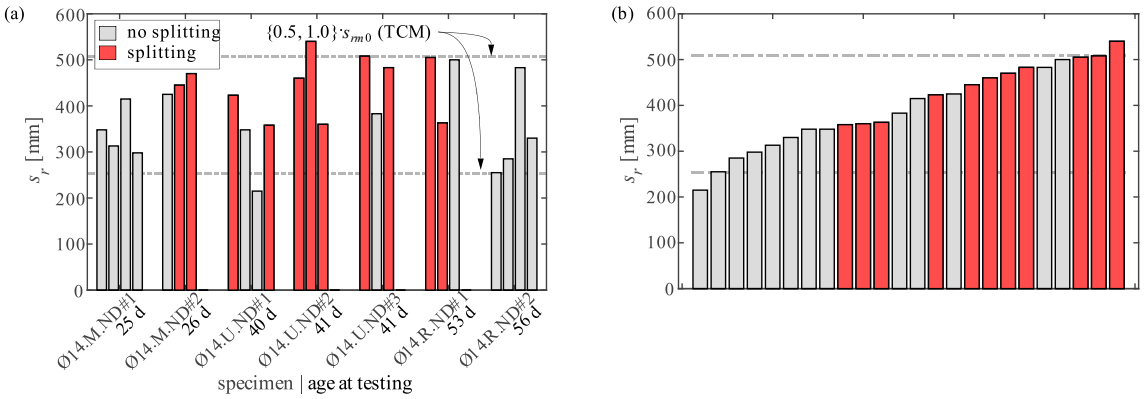

Fig. 11. Crack spacing with splitting occurrence for the specimens with Ø14 mm bars: (a) sorted by specimen and age at testing; (b) in ascending order.

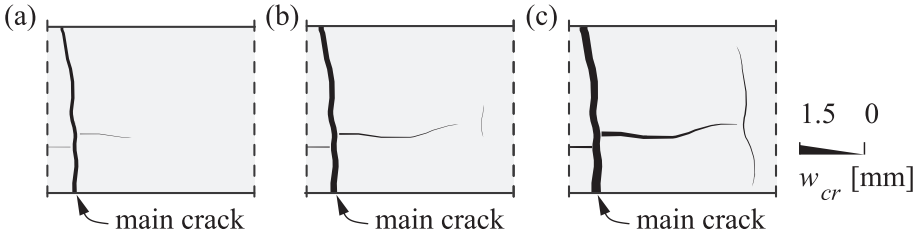

Fig. 12. Formation of longitudinal splitting and secondary transverse cracks with increasing load from (a) to (c). ACDM results of the front DIC of Ø16.M.HD#2 from x = 980 to 1150 mm.

yield strain was reached, remaining fairly constant after that. The splitting of these specimens was completed when steel strains at the crack reached about 5‰.

The behaviour in the plastic range of the specimens with normal-strength reinforcement varied significantly depending on the bar diameter. The average bond stresses of the Ø20 mm bar dropped quite abruptly to ca. 40% of the peak value and remained fairly constant during yielding. This observation can be explained by the fact that the splitting of this specimen was completed in the nonlinear elastic range, even before the peak bond stress was reached. However, in the specimen with the Ø16 mm bar, the average stresses dropped progressively during yielding since progressive splitting during the plastic range occurred in this case (until the steel strains reached 10‰ at the cracks, see Section 5.4.2). For the smallest bar diameter (Ø14 mm), no significant splitting was observed, and the average bond stresses decreased by only 20% in the plastic range. Then, the application of unloading and reloading cycles decreased the average bond stresses by another 23% relative to the peak load (see Section 5.5 for further discussion).

In Annex C, Fig. 24, one additional specimen of each configuration is evaluated. The specimen Ø20.U.ND#1 was unloaded and reloaded in the elastic range. As can be expected, this cyclic loading caused a reduction of the maximum average bond stress compared to the identical, but monotonically loaded specimen Ø20.M.ND#1 – i.e. by 27% ($1.0 \cdot f_{ct}$) (see also Section 5.5). However, the average bond stresses of Ø14.M.ND#1 were much lower than those of Ø14.U.ND#3, i.e. only $0.85 \cdot f_{ct}$. Ø14.M.ND#1 had one crack more and shorter crack spacings. These results indicate that Ø14.M.ND#1 might not be a reliable test and is thus not further discussed (see details in Annex C). Ø16.M.ND#1 and Ø16.M.HD#1 had similar average bond stresses as Ø16.M.ND#2 and Ø16.M.HD#2 (see Fig. 24).

The experimental observations indicate that the average bond stresses are highly sensitive to the reinforcement strains and thus also to the reduction of its tangent stiffness; they reached their peak for around 2‰, which coincides for normal-strength steel with the linear limit strain, and subsequently decreased with increasing deformation. With increasing bar diameter, the peak average bond stresses decreased and the post-peak bond deterioration was more pronounced, which confirms observations made by other authors [28]. The bond deterioration also correlates with the amount of CE parts exhibiting splitting, i.e. only 2 out of 6 for Ø14.U.ND#3, but 6 out of 8 for Ø20.M.ND#1, 10 out of 12 for Ø16.M.ND#2 10 and 5 out of 8 for Ø16.M.HD#2, as the latter three suffered a much more pronounced post-peak bond deterioration.

Finally, the commonly assumed average bond stresses of 1.8, or $2.0 \cdot f_{ct}$ assumed in the elastic range by the Eurocode 2 (EN 1992-1-1 2004) and the *fib* Model Code 2010, or the SIA 262, respectively, could not be confirmed by the experiments. The observed peak average bond stresses amounted to around $1.5 \cdot f_{ct}$, with even lower values on average over the entire elastic range.

5.4. Occurrence and relevance of splitting cracks

The experimental results presented in the last section highlight that the occurrence of splitting has a key impact on the bond behaviour. This aspect is investigated in more detail in the following, considering potential influencing factors such as the crack spacing, local bond and concrete stresses in the absence of a confining reinforcement that would prevent spalling.

5.4.1. Correlation between crack spacing and splitting

All specimens with a reinforcing bar diameter Ø ≥ 16 mm exhibited splitting regardless of age at testing (shrinkage) and crack spacing. The specimens with Ø14 mm bars did not always split, and a correlation between splitting and crack spacing could be observed. This is illustrated by Fig. 11, which shows the crack spacings with an indication of splitting within the CE (observed at the surface) in red, sorted by (a) age at testing and (b) crack spacing. Clearly, splitting is more frequent at larger crack spacings. All crack spacings were within the bounds predicted by the TCM (grey, dash-dotted lines). The graph could suggest that the crack spacing is quite important for the development of splitting cracks: all specimens with only two cracks split, while two out of three specimens with three cracks had no splitting at all and the third one only in two out of four sections between two cracks.

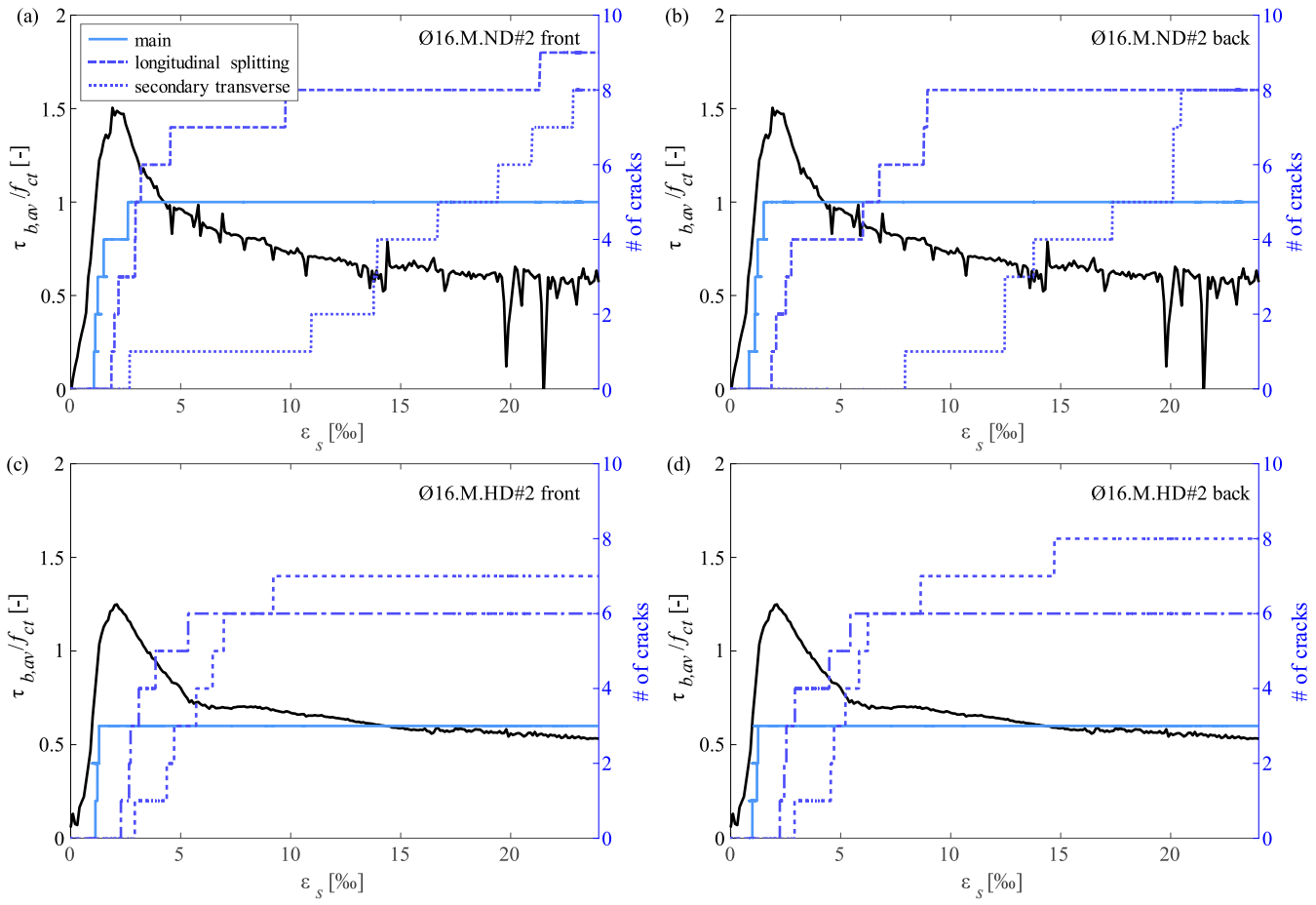

Fig. 13. Development of average bond stresses and number of main cracks, axial splitting cracks, and secondary transverse cracks against the steel strain at the crack for the crack pattern of Ø16.M.ND#2 at (a) the front and (b) the back, and for Ø16.M.HD#2 at (c) the front and (d) the back. Crack kinematics were determined from the DIC data using the ACDM software.

5.4.2. *Crack development after yielding*

Depending on reinforcement ratio, confinement, crack spacing, and material characteristics, longitudinal splitting and secondary transverse cracks will form. In the tests, it could be observed that longitudinal splitting cracks originated from the main cracks and subsequently, with increasing deformation, secondary transverse cracks formed at the tip of the longitudinal cracks (see Fig. 12).

The crack development in the plastic range is investigated by means of Fig. 13, which shows the average bond stresses (mean value of all CE) against the steel strains at the crack for Specimens Ø16.M.ND#2 and Ø16.M.HD#2. The number of through-cracks registered by the back (left) and front DIC systems (right) is plotted on the left ordinate, and cracks are categorised as main, longitudinal splitting, and secondary. The latter correspond to transverse cracks induced by splitting. All main cracks formed in the linear elastic range; NB the Ø20 mm normal-strength steel bar completed splitting before the plastic stage.

In Specimen Ø16.M.ND#2 (normal-strength steel, Fig. 13a-b), all main cracks but one formed in the linear elastic range. A first longitudinal splitting crack appeared on the front side before the last main crack had formed. Bond stresses dropped significantly only after several longitudinal splitting cracks had formed and progressed gradually while more such cracks formed (until $\varepsilon_s \approx 10‰$). Most secondary transverse cracks started forming after that, while bond stresses kept decreasing. In Specimen Ø16.M.HD#2 (high-strength steel, Fig. 13c-d), main cracks formed in the elastic and plastic range (until $\varepsilon_s \approx 5‰$). Longitudinal splitting cracks appeared after all main cracks had formed, accompanied by an abrupt decrease of the bond stresses. Finally, secondary transverse cracks appeared without a clear effect on bond stresses.

Established bond models determine the formation of new cracks based on the tensile concrete stresses (transferred by bond) and postulate a decrease of bond stresses after yielding. Hence, they cannot explain the observed crack formation in the plastic range; this concerns both main cracks as well as splitting cracks if the radial compressive stresses causing splitting are related to the bond shear stresses. The results suggest that splitting is rather related to the deformations of the reinforcing bar than the bond stresses, and checking compatibility at the steel-to-concrete interface could explain and help predict cracking in the plastic range. However, the formation of splitting cracks was completed at lower strains in the specimen with a high-strength but low-stiffness reinforcing bar, indicating that local steel strains are not the only factor influencing splitting. As discussed in Section 5.2, the larger crack spacings and higher concrete tensile stresses in the high-strength specimen could also have affected the splitting behaviour.

5.4.3. *Influence of splitting on local and average bond stresses*

The differences in the local bond behaviour between parts with and without splitting cracks are examined in the following for the $CE_{3,inf}$ (no splitting) and $CE_{5,inf}$ (splitting) of Specimen Ø16.M.ND#2 (see Fig. 9a, left) for a direct comparison of the behaviour in both cases. Fig. 14 illustrates the development of (a) the concrete tensile stress profile and (b) the local bond stress profile over the length of the CE parts, as well as (c) the bond stress-slip (steel elongation) relationship with increasing load.

Both CE parts were initially bounded by a section I defined by constant steel strains and became considerably shorter at the formation of a neighbouring crack; beyond this point, their length was defined by the

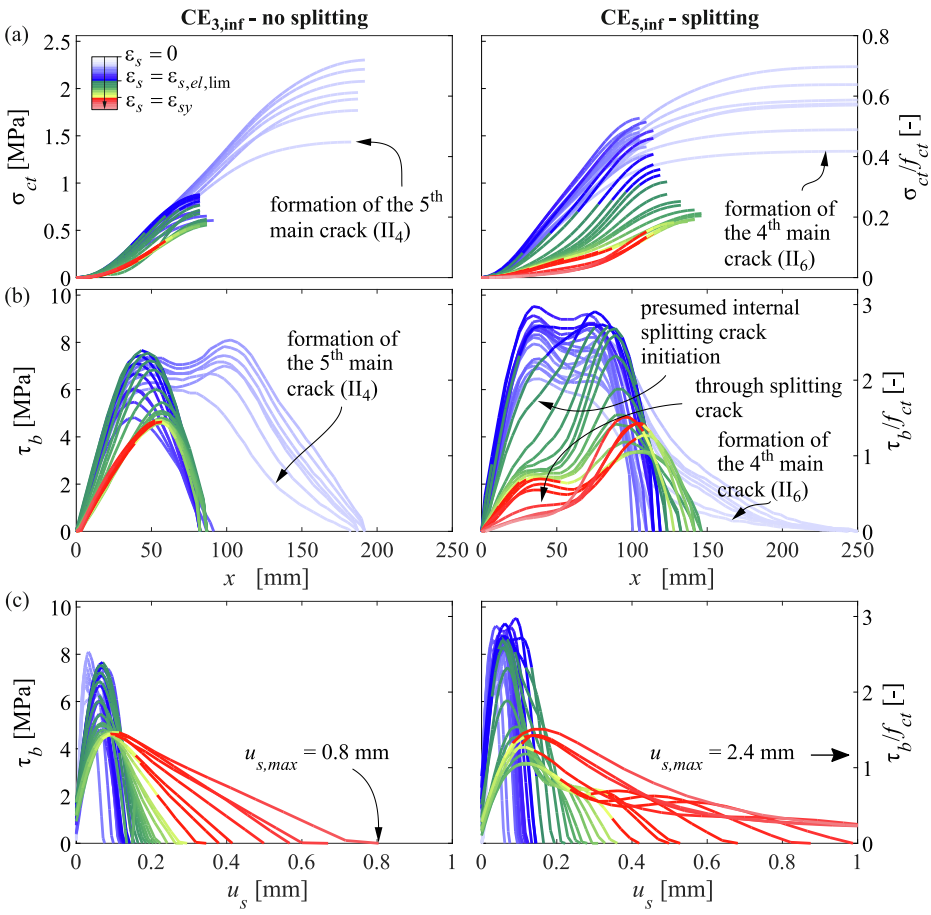

Fig. 14. Comparison of the bond behaviour in CE parts without (left) and with (right) splitting cracks of specimen Ø16.M.ND#2: (a) concrete tensile stresses (x denotes the distance to the crack); (b) bond shear stresses; (c) bond shear stress as a function of the steel elongation (the colour-mapping denotes the local steel strains with blue: linear elastic, green: nonlinear elastic, and red: plastic). (For interpretation of the references to colour in this figure legend, the reader is referred to the web version of this article.)

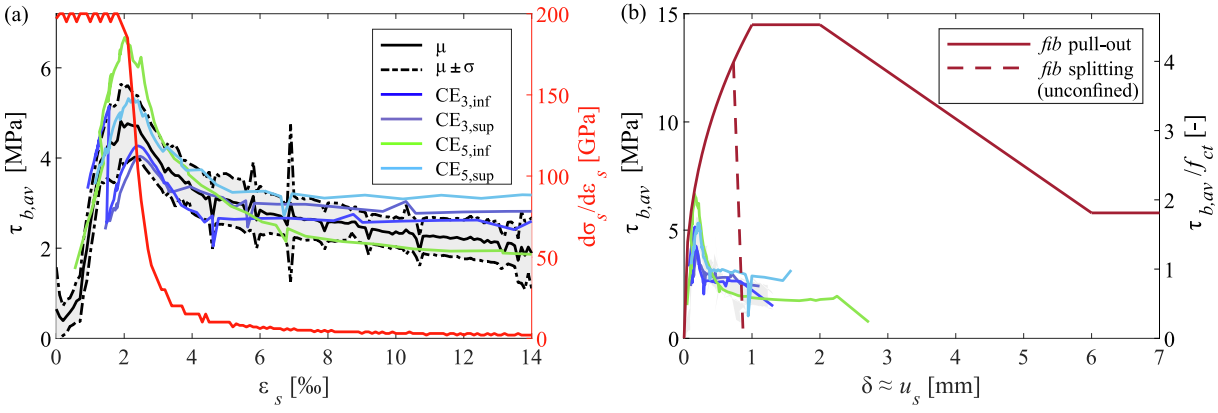

Fig. 15. Average bond stresses of $CE_{3,inf}$, $CE_{3,sup}$, and $CE_{5,sup}$ (no splitting) and $CE_{5,inf}$ (splitting): (a) against steel strains at the crack, compared to the mean behaviour and standard deviation of Specimen Ø16.M.ND#2; (b) against slip, compared to the fib Model for Code for Concrete Structures 2010 [32].

location of bond stress reversal. The maximum concrete tensile stresses were very similar in both CE parts (~$0.7{\cdot}f_{ct}$) before the formation of the neighbouring main crack, dropping significantly upon its formation as the transfer lengths shortened while the local bond stresses remained similar. At the end of the linear elastic range, $CE_{5,inf}$ that would split at a later stage had a longer transfer length (105 vs 82 mm of $CE_{3,inf}$) and higher peak bond stresses (2.91 vs $2.39{\cdot}f_{ct}$), which resulted in more than twice as high maximum concrete tensile stresses (0.53 vs $0.25{\cdot}f_{ct}$). The splitting of $CE_{5,inf}$ in the plastic stage could thus have been triggered by its higher peak bond shear stresses, longer transfer length, and higher concrete tensile stresses compared to $CE_{3,inf}$, which did not split.

As already observed in Sections 5.2 and 5.3, the local transition to the nonlinear elastic range caused a distinct decrease in the local peak and average bond stresses in both specimens. The decline was more significant in $CE_{5,inf}$ since simultaneous splitting occurred (47% drop with respect to 40% for the CE parts without splitting). The decrease in bond stresses was accompanied by an increase in the length of $CE_{5,inf}$ exhibiting splitting (consuming parts of the neighbouring element $CE_{5,sup}$, which did not split), while the length of $CE_{3,inf}$ without splitting (like the neighbouring $CE_{3,sup}$) remained fairly constant. The reinforcement elongation, which roughly corresponds to the slip (see Eq. (5)), was three times larger for the CE part without splitting (2.4 vs 0.8 mm).

Evidently, splitting affects not only the local but also the average bond stresses, as highlighted in Section 5.3 by comparing the average

Table 8
Characteristic values of local and mean bond behaviour for each CE of specimens Ø14.U.ND#3, Ø20.M.ND#1, Ø16.M.ND#2, and Ø16.M.HD#2.

Specimen and CE		$\tau_{b,av,max}$ [MPa]	$\tau_{b,av,max} / f_{ct}$ [–]	$\tau_{b,av,max} \cdot \pi \cdot Ø$ [kN/m]	$\tau_{b,max}$ [MPa]	$\tau_{b,max} / f_{ct}$ [–]	$\sigma_{ct,max}$ [MPa]	$\sigma_{ct,max} / f_{ct}$ [–]	CE length (post-peak) [mm]	Splitting
Ø14.U.ND#3	$CE_{1,inf}$	4.40	1.51	194	8.72	2.99	2.48	0.85	235	no
	$CE_{1,sup}$	5.09	1.74	224	9.60	3.29	**2.52**	**0.86**	285	yes
	$CE_{2,inf}$	4.61	1.58	203	8.16	2.79	2.23	0.76	195	no
	$CE_{2,sup}$	4.84	1.66	213	**12.17**	**4.17**	1.71	0.59	185	no
	$CE_{3,inf}$	**5.41**	**1.85**	**238**	10.60	3.63	2.35	0.80	275	yes
	$CE_{3,sup}$	4.18	1.43	184	7.55	2.58	2.22	0.76	220	no
Ø20.M.ND#1	$CE_{1,inf}$	3.35	1.15	211	5.14	1.76	1.57	0.54	170	yes
	$CE_{1,sup}$	4.17	1.43	262	7.29	2.50	2.06	0.71	145	yes
	$CE_{2,inf}$	4.14	1.42	260	7.46	2.56	**2.50**	**0.86**	155	yes
	$CE_{2,sup}$	**4.21**	**1.44**	**264**	6.96	2.38	2.11	0.72	170	yes
	$CE_{3,inf}$	3.29	1.13	207	5.96	2.04	1.44	0.49	120	no
	$CE_{3,sup}$	3.59	1.23	226	6.46	2.21	2.40	0.82	165	yes
	$CE_{4,inf}$	4.04	1.38	254	**7.79**	**2.67**	2.47	0.85	300	yes
	$CE_{4,sup}$	3.45	1.18	217	4.97	1.70	2.02	0.69	120	yes
Ø16.M.ND#2	$CE_{1,inf}$	5.50	1.72	276	**13.08**	**4.09**	1.84	0.57	114	yes
	$CE_{1,sup}$	5.29	1.65	266	10.04	3.14	1.91	0.60	178	yes
	$CE_{2,inf}$	4.47	1.40	225	9.75	3.05	1.93	0.60	132	yes
	$CE_{2,sup}$	4.49	1.40	226	11.66	3.64	1.11	0.35	87	no
	$CE_{3,inf}$	5.15	1.61	259	11.42	3.57	2.33	0.73	87	no
	$CE_{3,sup}$	4.05	1.27	204	11.03	3.45	0.92	0.29	87	no
	$CE_{4,inf}$	5.03	1.57	253	12.53	3.92	1.45	0.45	119	yes
	$CE_{4,sup}$	5.55	1.73	279	10.95	3.42	**2.48**	**0.77**	137	yes
	$CE_{5,inf}$	**6.80**	**2.13**	**342**	12.81	4.00	2.28	0.71	137	yes
	$CE_{5,sup}$	5.50	1.72	277	11.93	3.73	1.67	0.52	96	no
	$CE_{6,inf}$	5.31	1.66	267	10.03	3.14	1.78	0.56	142	yes
	$CE_{6,sup}$	4.34	1.36	218	10.74	3.36	1.99	0.62	174	yes
Ø16.M.HD#2	$CE_{1,inf}$	3.75	1.17	188	6.66	2.08	1.48	0.46	117	yes
	$CE_{1,sup}$	4.14	1.29	208	8.41	2.63	1.41	0.44	150	yes
	$CE_{2,inf}$	4.42	1.38	222	7.71	2.41	1.94	0.61	163	yes
	$CE_{2,sup}$	4.23	1.32	212	6.85	2.14	1.63	0.51	157	yes
	$CE_{3,inf}$	4.33	1.35	218	6.61	2.07	2.07	0.65	176	no
	$CE_{3,sup}$	**4.46**	**1.39**	**224**	7.46	2.33	2.10	0.66	228	yes
	$CE_{4,inf}$	4.39	1.37	220	**9.02**	**2.82**	**2.43**	**0.76**	101	yes
	$CE_{4,sup}$	0.95	0.30	48	1.97	0.62	0.05	0.02	13	yes
	$CE_{5,inf}$	3.39	1.06	170	5.60	1.75	1.22	0.38	160	yes
	$CE_{5,sup}$	4.07	1.27	205	7.91	2.47	2.34	0.73	225	no

behaviour of specimens with and without splitting. This analysis is complemented in the following by comparing the average bond stresses of CE parts with and without splitting of a single specimen to enable a direct comparison. Fig. 15a shows the average bond stresses of CE_3 and CE_5 of Specimen Ø16.M.ND#2 and the comparison to the statistical values of all twelve CE parts of this specimen already shown in Fig. 10e, including the tangent stiffness of the reinforcing steel. Within these CE parts, splitting was observed only in $CE_{5,inf}$ (green curve). $CE_{5,inf}$ had average bond stresses higher than the mean behaviour plus the standard deviation in the elastic range. Upon splitting in the plastic range, the average bond stresses of $CE_{5,inf}$ dropped to the range of the mean minus the standard deviation. The decrease was significantly less pronounced in the elements without splitting in the plastic range (blue curves), with the average bond stresses at high strains in the range of the mean plus standard deviation. The loss of average bond stresses of $CE_{3,inf}$ from 5.2 to 2.6 MPa (1.61 to $0.8 \cdot f_{ct}$) in the linear elastic range is related to the formation of a neighbouring crack and a new CE part ($CE_{3,sup}$), rendering $CE_{3,inf}$ much shorter. $CE_{3,inf}$ and $CE_{3,sup}$ exhibited distinctly lower average bond stresses than $CE_{5,sup}$, which also did not split but is much longer (see Fig. 9 left). In Fig. 15b, the bond stress-slip behaviour of these crack elements is compared to the *fib* Model Code 2010 prediction for local bond behaviour [32]. The *fib* Model Code predicts much higher bond stresses and a very high slip at splitting. The ascending branch is modelled with an accurate stiffness.

The results highlight that splitting affected the post-peak average bond stress behaviour in this case, though less pronouncedly than suggested by the *fib* Model Code 2010. The split crack element part has only slightly lower residual peak bond stresses than the ones that did not split. A considerable influence could be observed in the peak value of the average bond stresses. Other than predicted by the *fib* Model Code 2010, elements exhibiting splitting had higher peak values than elements that did not split. If the crack spacing was high, larger bond and concrete tensile stresses developed and splitting was more likely, while shorter CE parts had smaller bond stresses and did not split. Despite the reduction in the bond stresses, crack widths were still smaller in the short elements due to the shorter length over which steel strains are integrated.

5.4.4. *Influence of the bar diameter*

The discussions in the previous subsections focussed on a single specimen, which facilitates a direct comparison of CE exhibiting splitting or not, but does not allow to assess the effect of the reinforcing bar diameter nor the reinforcement ratio. In order to give further insights into the influence of splitting on the bond and crack behaviour, this section compares the results of tests with different bar diameters and reinforcement ratios. Note that these two effects are coupled in the experiments of this study since the concrete cross-section was kept constant, such that their influence cannot be investigated independently.

Table 8 shows characteristic results of the local and average bond behaviour of Specimens Ø14.U.ND#3 (only monotonic part), Ø20.M.ND#1, Ø16.M.ND#2 and Ø16.M.HD#2, including the maximum average bond stresses $\tau_{b,av,max}$, the maximum local bond stresses $\tau_{b,max}$, and the maximum concrete tensile stresses $\sigma_{ct,max}$. The average and local bond stresses of different CE parts are similar within one specimen but vary between the four specimens. The maximum bond stress of an element (marked in bold in Table 8) varied between $1.44 \ldots 2.13 \cdot f_{ct}$ in terms of average bond stresses and $2.67 \ldots 4.17 \cdot f_{ct}$ in terms of local bond stresses. However, the maximum concrete tensile stresses were very similar, in the range $0.76 \ldots 0.86 \cdot f_{ct}$.

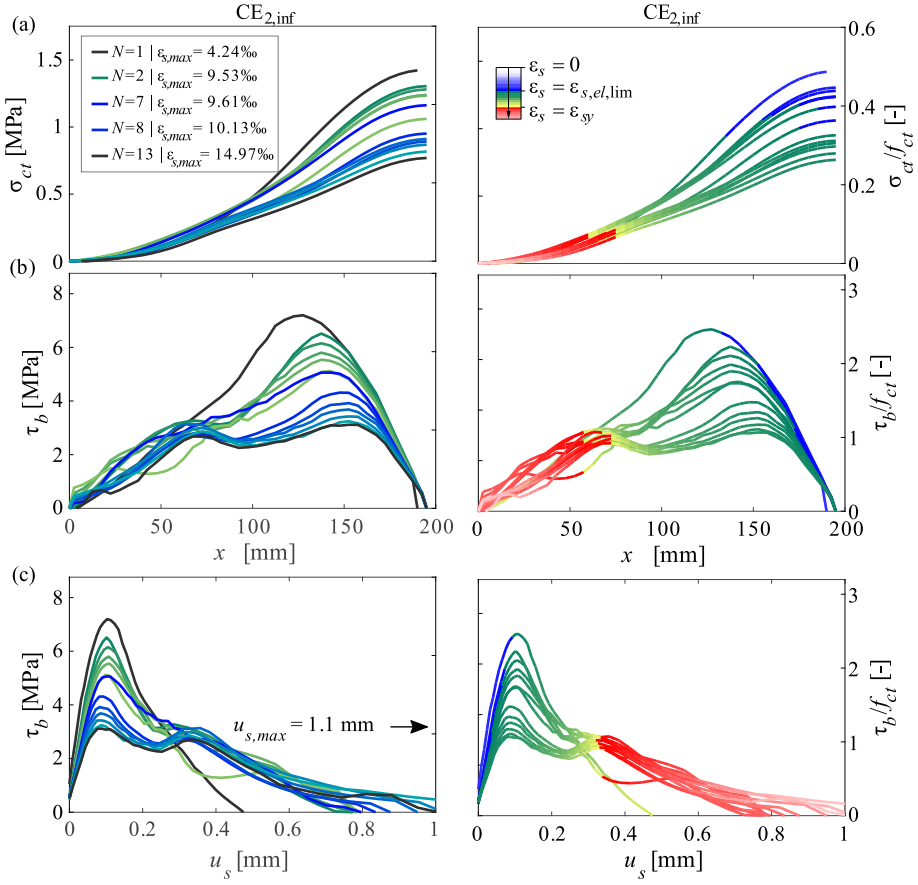

Fig. 16. Influence of unloading and reloading cycles and increasing experienced maximum strain (left) and local strains (right) on the local bond behaviour for $CE_{2,inf}$ of Ø14.U.ND#3 (F = 80 kN): (a) concrete tensile stresses; (b) local bond stresses; (c) local bond stress – steel deformation relationship (x denotes the distance to the crack; the colour-mapping corresponds to the cycle number as in Fig. 22a, while on the right it indicates the local reinforcement strain with blue: linear elastic, green: nonlinear elastic, and red: plastic). (For interpretation of the references to colour in this figure legend, the reader is referred to the web version of this article.)

The last column indicates whether splitting occurred. Ø14.U.ND#3 had much higher local and average bond stresses than Ø20.M.ND#1 and larger crack spacings but nevertheless exhibited clearly less splitting. Therefore, the magnitude of local and average bond stresses in the elastic range alone are no reliable indicators for splitting, even when the concrete geometry and properties are identical (see Annex D for proof). The reinforcement ratio, or bar diameter in this case, is an equally significant factor for splitting; this can be explained by the observation that the load transferred to the concrete per unit length ($\tau_{b,av,max}\cdot\pi\cdot Ø$) is proportional to the bar diameter. Therefore, bars of smaller diameters can transfer higher bond stresses without causing splitting. On the other hand, the results confirm the relevance of the crack spacing (see also Section 5.4.1): for larger crack spacings, bond stresses and concrete tensile stresses tend to be higher. The combination of large crack spacing and high concrete stresses appears to be decisive for splitting (see last three columns of Table 8).

5.5. *Influence of cyclic loading*

5.5.1. *Unloading and reloading with plastic steel deformations*

Bond is not only affected by increasing loading and splitting but also by repeated unloading and reloading (UR) cycles, which is discussed in the following. The distribution of concrete tensile stresses, bond shear stresses, and the bond stress-steel elongation behaviour in $CE_{2,inf}$ for Ø14.U.ND#3 (see Fig. 22a, Table 1, and Fig. 8a, left) are investigated (N = 13 is the final loading cycle prior to loading until failure). The results for a load F = 80 kN during (re)loading are shown in Fig. 16. The right and left parts of the figure differ only in the information given by the colour map, which on the left and right side denotes the cycle number and local reinforcement strain, respectively. The maximum steel strain $\varepsilon_{s,max}$ at the crack of the entire loading history (indicated for each cycle in the left legend) is observed to increase significantly with the applied cycles. At the same load, very different bond stresses and slips are observed, depending on the maximum deformation and the number of cycles that had preceded: while $\varepsilon_{s,max}$ increases only marginally between the 2nd and the 7th cycle, the peak average bond shear stress decreases from 6.5 MPa to 5.0 MPa (–23%), whereas the slip (steel elongation) increases only marginally from 0.77 to 0.79 mm. In the regions where the reinforcement was in the nonlinear elastic range, the bond deteriorated drastically with the cycles (from 7.2 to 2.2 MPa), while the maximum experienced strain at the crack grew from 4.24 to 14.97‰ despite that the local strains did not change much between the cycles. These observations indicate that the deterioration of bond can be attributed to the influence of loading and unloading and to the increase in $\varepsilon_{s,max}$. Two mechanical phenomena could explain this observation: (i) the formation and progression of internal cracks with increasing steel deformations, reducing the bearing capacity of the concrete by reducing and eventually impeding the formation of multiaxial stress states ensuring confinement, and (ii) the progressive local concrete crushing in front of the ribs (see Fig. 7a), with the concrete disintegrating upon decompression when the specimen is unloaded, thereby irreversibly deteriorating the load transfer. These observations are in accordance with the observed reduction of the average bond stresses (-30%) during the cyclic loading (see Section 5.3 and Fig. 10c).

The response of Specimen Ø14.U.ND#3 during one unloading cycle is discussed in the following. Fig. 17 shows the steel strains and elongations for the 7th unloading (i.e. from F_{sup} = 85 kN to F_{inf} = 1 kN) along the specimen, excluding the edge parts. Fig. 17a and c illustrate the strains and slip at selected load levels upon reducing the load from F_{sup} to F_{inf}, and Fig. 17b and d show the changes relative to the state at F_{sup}. After complete unloading, residual strains remained even in the linear elastic regions (e.g. at 835 mm). It can be seen that the bar unloaded over the entire length (and not only close to the crack) right from the beginning of the unloading branch. Determining bond stresses during

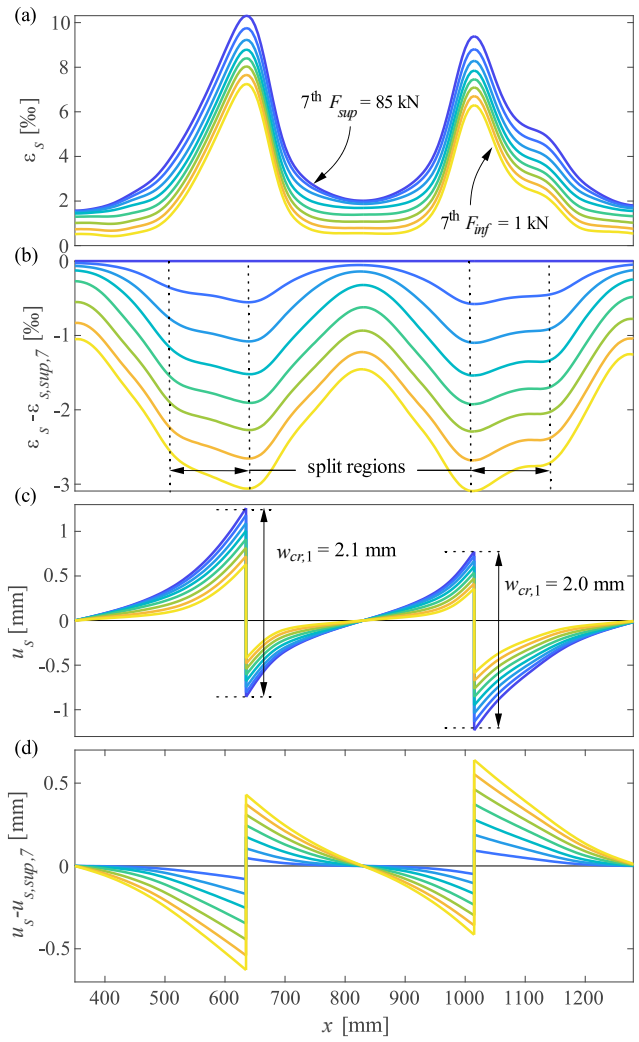

Fig. 17. The 7th unloading of Specimen Ø14.U.ND#3 from 85 to 1 kN: (a) steel strains; (b) difference in steel strains relative to the upper load; (c) steel elongation; (d) difference in steel elongation relative to the upper load.

cyclic loading including plastic steel strains is very challenging. The exact unloading and reloading constitutive relationship of the reinforcement subjected to plastic deformations would have to be known [8]. While it would be highly interesting, such analyses are beyond the scope of this paper. Nonetheless, as confirmed by Fig. 17c, it can be concluded that slip reversal (i.e. a decrease of absolute slip) did not initiate at the cracks and progress towards the centre of the CE as postulated by common bond models for unlading [41,42] but occurred over the entire CE length simultaneously.

Due to the reversal of bond stresses, the reduction in the steel strains upon unloading was higher at the crack than in the centre between cracks (see Fig. 17b), though the difference is relatively small, indicating low bond stresses resisting the slip reversal. The regions with splitting cracks, ranging from 520 to 635 mm and from 1005 to 1150 mm, unloaded similarly to the cracked cross-section, indicating that even smaller bond stresses due to longitudinal splitting might have occurred.

5.5.2. *Unloading and reloading with elastic steel deformations*

This section analyses the response of Specimen Ø20.U.ND#1, in which the reinforcement remained elastic upon unloading and reloading over its entire length, thus avoiding the issues of cyclic loading in the plastic range. Fig. 18 shows the results of the first unloading from F_{sup} = 130 to F_{inf} = 0 kN over the length of $CE_{2,sup}$ and $CE_{3,inf}$. Prior to this unloading, six cycles with F_{sup} = 35 kN and F_{inf} = 0 kN were applied

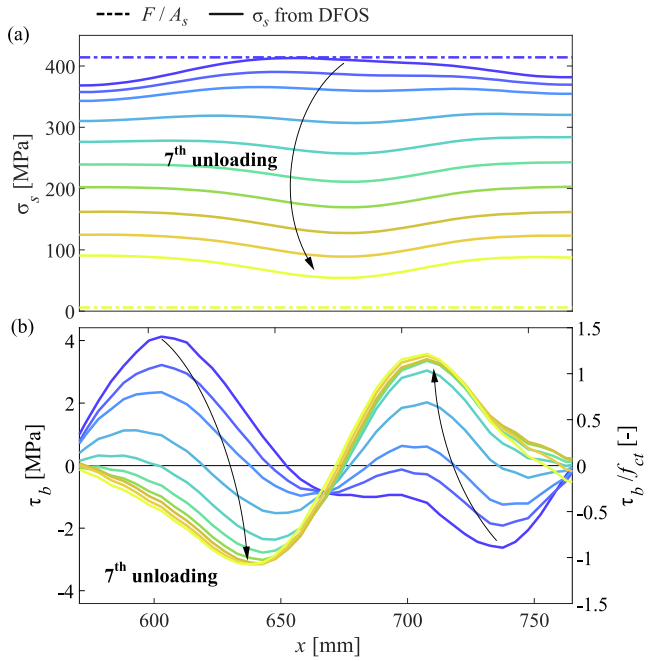

Fig. 18. First unloading of two CE adjacent to a crack of specimen Ø20.U.ND#1 from 130 kN to 0 kN(preceded by six cycles in the uncracked state as shown in Fig. 22b): (a) steel stresses; (b) local bond stresses.

where in the 2nd cycle, a first crack had formed (see Fig. 22b). The bond stress distribution (Fig. 18b) shows that upon unloading, the sign of the bond stresses initially changed near the cracks and only later, at a stress below about 300 MPa, over the entire length. These observations confirm the modelling assumptions that, during unloading, the reinforcing bar moves back towards its original position (slip reversal with decrease of absolute slip) and the sign of bond stresses is reversed over a growing length with decreasing load [41,42].

Another observation is the residual stress state after unloading: Assuming that the cracks are stress-free, the theoretical steel stresses at the crack F/A_s (dashed curves in Fig. 18a) should be 6 MPa at the lower load F_{inf} = 0 kN (which was not exactly zero to ensure avoiding compression), but effectively amounted to 54 MPa. Between the cracks, even higher residual steel stresses around 90 MPa were observed. While the latter can be explained by reversed bond stresses caused by slip reversal [41], the residual tensile stresses at the crack indicate that the cracks did not close entirely, causing compression on the crack surface and tension in the reinforcing bar (crack closure effect [43,44]). The residual steel stresses at the cracks further complicate the determination of the cyclic behaviour, as the steel stresses at the cracks cannot be determined by equilibrium assuming stress-free cracks.

The effect of cycles in the elastic range was similar to that observed in the plastic steel range (Section 5.5.1). Fig. 19 a illustrates this observation in a boxplot of the average bond stresses of Ø20.U.ND#1 during ten cycles between F_{sup} = 130 and F_{inf} = 0 kN. At the first loading to F_{max}, the median of all ten CE was 2.4 MPa = 0.81·f_{ct}. After only one cycle, it decreased by 12% to 2.1 MPa = 0.71·f_{ct}. After ten cycles, the median was 35% lower at 1.5 MPa = 0.53·f_{ct}, while the scatter of average bond stresses over the tension chord had slightly decreased. No significant additional bond degradation was observed between the 8th and 10th cycle. Fig. 19b illustrates the bond stress distribution of $CE_{2,sup}$ and $CE_{3,inf}$ during the ten cycles (same x-range as in Fig. 18 for comparison). Local deterioration of bond stresses is visible over the entire transfer length, being most pronounced near the local peak of $CE_{2,sup}$, where local bond stresses were very high upon first loading.

For Specimen Ø20.U.ND#1, the peak in the average bond stresses was as low as 1.0·f_{ct}, and was reached at a steel stress at the crack of

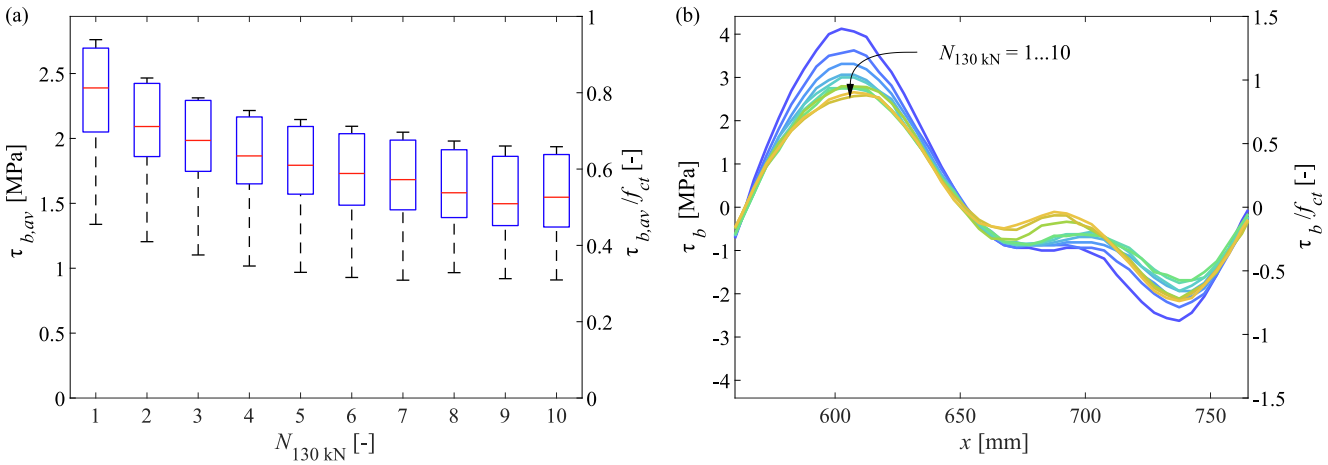

Fig. 19. Mean bond degradation of $CE_{2,sup}$ and $CE_{3,inf}$ of Ø20.U.ND#1 during 10 cycles with an upper load of 130 kN and a lower load of 0 kN: (a) boxplot; (b) local bond stress distribution.

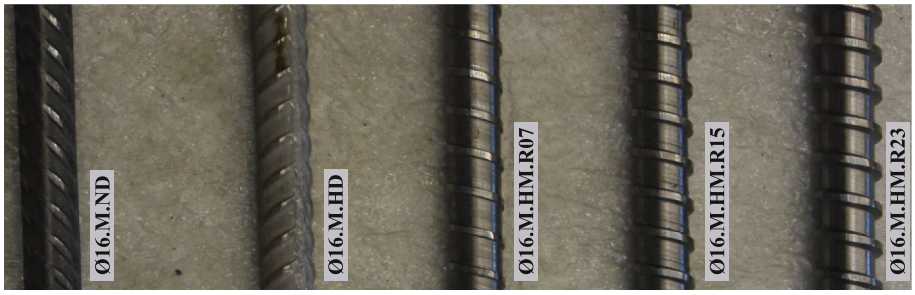

Fig. 20. Rib patterns of the reinforcing bars of Series 2.

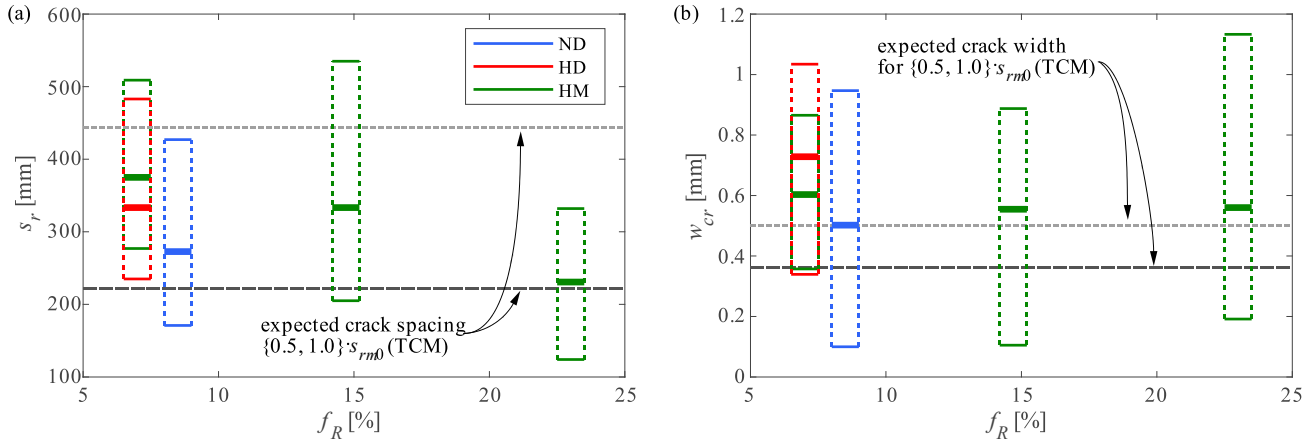

Fig. 21. Influence of the relative rib area f_R and the steel bar type on the crack behaviour of Series 2 (Ø16 mm, ρ = 0.89%): (a) minimum, average, and maximum crack spacing with limits of theoretical crack spacing according to the Tension Chord Model (TCM) [29]; (b) minimum, average, and maximum crack widths at a steel stress of $F/A_s \equiv \sigma_{s,adm}$ = 430 MPa, predicted by the TCM (Note: this stress corresponds to the maximum expected crack width of 0.5 mm according to SIA 262 [30]).

$\sigma_{s,max}$ = 335 MPa (see Fig. 24b), i.e. after the cycles in the uncracked state and prior to its first loading to $F_{sup,2}$ = 130 kN ($\sigma_{s,max}$ = 413 MPa) and the second set of cycles. Meanwhile, the maximum average bond stress of the monotonically loaded Specimen Ø20.M.ND#1 amounted to 1.27·f_{ct} (see Fig. 10). This indicates that the unloading and reloading in the uncracked stage at $F_{sup,1}$ = 35 kN ($\sigma_{s,max}$ = 111 MPa) (when only one crack had developed) already caused a bond deterioration that is visible for higher loads.

A simple model accounting for the effect of unloading and reloading on bond could consist of a reduction factor for the average bond stresses (corresponding to 1/1.27 = 0.78 in Specimen Ø20.U.ND#1) over the entire transfer length. Such a factor (assuming a logarithmic decrease of the average bond stresses with the number of load cycles) has recently been proposed for fatigue loading in the elastic range [45]. However, further research is required to validate this approach and to consider other phenomena which have been observed to influence average bond stresses, such as the maximum steel strains of the loading history, splitting, and the bar diameter.

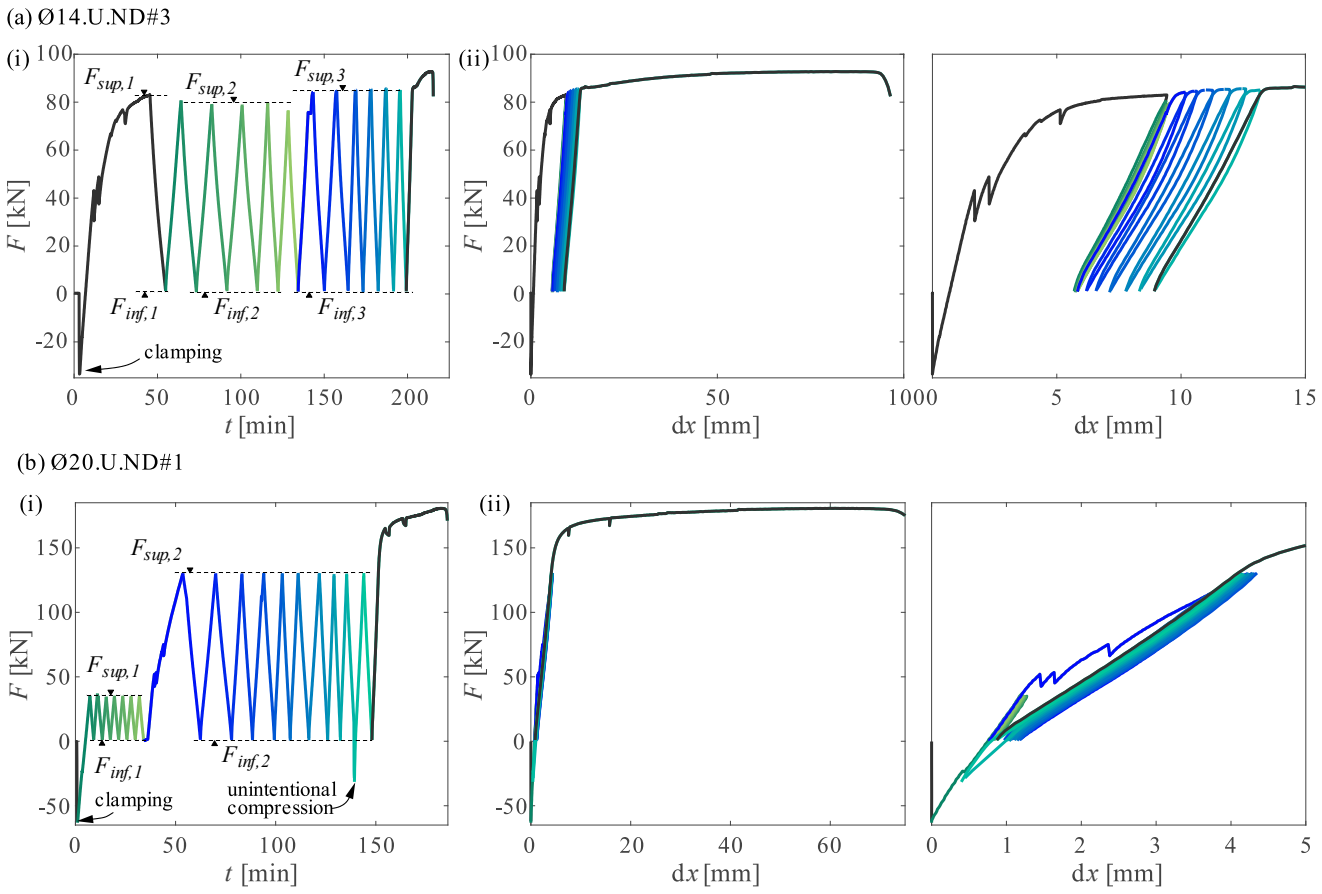

Fig. 22. Loading history of (a) Ø14.U.ND#3 and (b) Ø20.U.ND#1: (i) applied load over time and (ii) load-deformation behaviour of the RC ties.

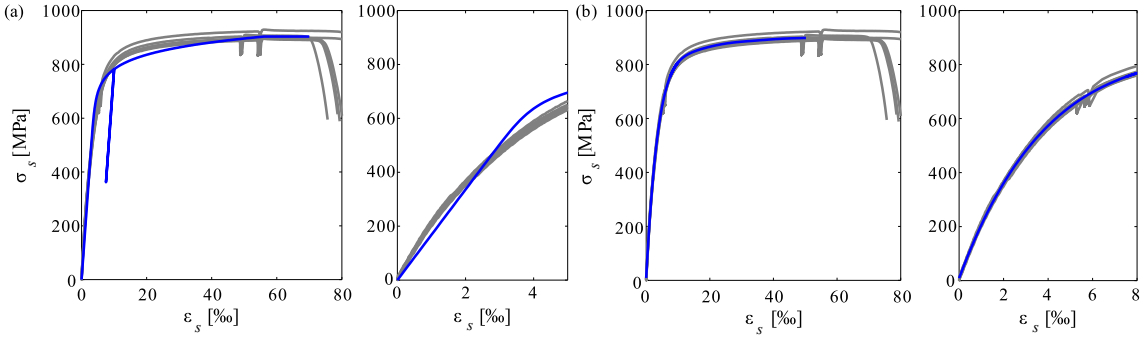

Fig. 23. Constitutive modelling of the high-strength deformed reinforcing bars: (a) Ramberg-Osgood equation; (b) eighth-order polynomial fit (blue) against test data of six direct steel tests (grey). (For interpretation of the references to colour in this figure legend, the reader is referred to the web version of this article.)

5.6. *Influence of rib geometry*

As discussed in Section 3, most bond models and current design codes do not account for the characteristics of the deformed reinforcing bars, i.e. the rib geometry, despite that it has been known to be a decisive parameter for more than a century [22]. In order to quantify the impact of neglecting the effect of the rib geometry, this section investigates its influence on the serviceability behaviour of the specimens of Series 2, which were cast with the same concrete and reinforced with bars of identical diameter but different relative rib areas and steel strength (see Table 2 and Fig. 20). As indicated in Section 4.1.3, only the maximum rib height of the reinforcing bars was measured, what hinders a precise estimation of the rib area for deformed bars with variable rib height (ND and HD). The visual inspection of the rib patterns of Series 2 allows estimating an average rib height in the order of 50…70% of the maximum value reported in Table 4. This leads to values of the relative area of ca. 8.5% for the Ø16 normal-strength deformed bar and to 7.0% for the Ø16 high-strength deformed bar (i.e. in the same order of magnitude than the machined bars with lower rib depth: R07).

Fig. 21 summarises the average crack spacings (a) and crack widths at a steel stress of 430 MPa (b) of all specimens of Series 2 as a function of the relative rib area and steel type. The theoretical maximum and minimum crack spacings predicted by the TCM (i.e. 50% and 100% of the theoretical maximum crack spacing s_{rm0}) when assuming E_s = 205 GPa are included in Fig. 21a. The stress of 430 MPa selected in Fig. 21b to calculate crack widths is a representative value for the SLS range (which corresponds to an expected maximum crack width of 0.5 mm according to the SIA 262 (2013) provisions [30]). Even though the crack spacings of all specimens were within the predicted range, all average crack widths were above the maximum predicted ones. The HD

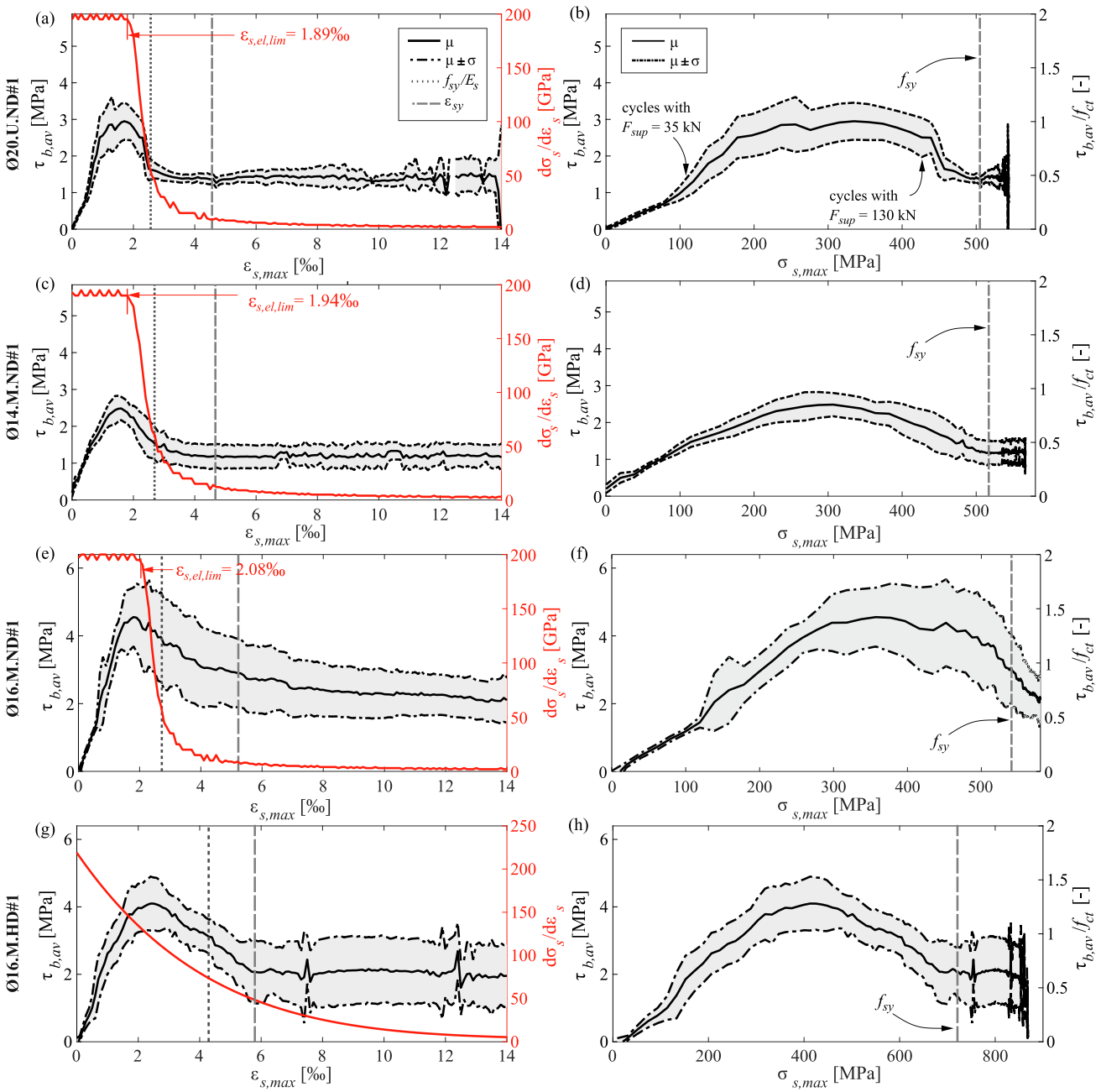

Fig. 24. Mean value and standard deviation of average bond stresses and tangent modulus of the bare steel with maximum steel strains and stresses: (a)-(b) Ø20.U.ND#1; (c)-(d), Ø14.M.ND#1; (e)-(f) Ø16.M.ND#1; (g)-(h) Ø16.M.HD#1.

specimens (deformed Top12 high-strength steel bars, $f_R \approx 7\%$, red) had a slightly smaller mean crack spacing than the HM-07 specimens (machined ETG88 high-strength steel bars, $f_R = 7\%$, green). However, the crack widths in the HD specimens were even larger, which can be attributed to the lower stiffness of the Top12 steel.

There is a clear trend of smaller crack spacings with higher relative rib areas, which could be beneficial for the crack behaviour. However, such a trend could not be confirmed for the crack widths, which were similar for all specimens despite the wide range of relative rib areas. Presumably, increasing the size of the ribs favoured the occurrence of splitting cracks in the elastic range, which led to a significant bond degradation counteracting the beneficial effect of the smaller crack spacing. Hence, to exploit the potential of bars with high relative rib areas to reduce crack widths, it is essential to provide sufficient confinement to avoid splitting and ensure higher bond stresses throughout the serviceability range, which is in agreement with previous observations [21,23–25]. As a side note, the crack widths at a stress of 430 MPa exceeded the nominal value of 0.5 mm expected according to SIA 262 for this stress level, which can be attributed to (i) the reduced bond stresses due to splitting and (ii) the generally lower bond stresses observed also in elements that do not split compared to design values. However, in practice, structural elements have transverse reinforcement, ensuring confinement and improving bond with respect to these RC ties.

6. Summary of the main findings and conclusions

Distributed fibre optical strain measurements (DFOS) and digital image correlation (DIC) are helpful tools to assess the structural behaviour of reinforced concrete structures and to validate models and

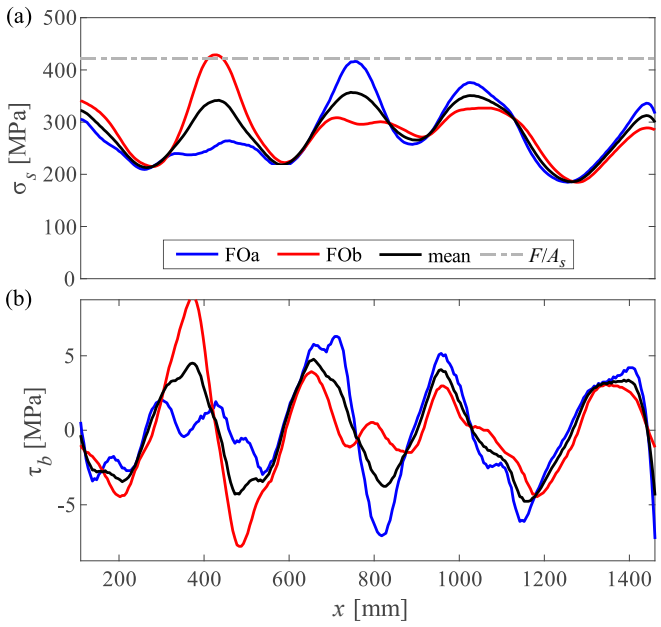

Fig. 25. Quality of the fibre optical measurement of specimen Ø14.M.ND#1 examined on (a) the steel stresses; (b) the derived bond stresses.

their underlying assumptions. In particular, DFOS has been established as a powerful tool to investigate bond in reinforced concrete structures in practice-relevant experimental setups. The instrumentation only minimally affects the bond behaviour, provides results with high resolution, and is relatively time- and cost-efficient compared to other methods. This study successfully applied both measurement technologies to investigate the local and average bond behaviour of 21 RC ties with varying bar diameters, steel grades, relative rib areas, and loading histories.

Although the distribution of bond stresses is not considered to be crucial for the calculation of global values such as crack spacing, crack widths, tension stiffening, and ductility, it is nevertheless important for the development of refined models as these results help to understand the failure modes and the load transfer mechanisms in general, and ultimately to quantify the average bond stress required for design purposes. The local measurements helped to understand the consequences on a local scale caused by load increase in general and specifically by yielding, cyclic loading, and splitting. While steel and bond stresses could readily be determined for the monotonically loaded specimens and the cyclic tests limited to elastic steel stresses with high accuracy and resolution, this proved more difficult in the case of unloading after plastic deformations due to uncertainties in the constitutive behaviour (the steel stiffness and the hysteresis while unloading and reloading vary with the applied plastic deformations). Further research is needed to determine bond stresses from DFOS measurements reliably and eventually model bond more realistically in such cases.

The experimental results highlighted that local and average bond stresses decrease starting with the nonlinearity of steel and on average reach values lower than those suggested by codes. In the linear elastic steel state, the local bond stress peak increases and moves away from the crack with increasing load while the bond stresses closer to the crack remain fairly constant. As the nonlinear range starts, the peak moves further towards the ideal cross-section and the bond stresses closer to the crack decrease. If splitting occurs, the peak and the slope decrease abruptly; the bond stresses might increase further away from the splitting crack again.

When comparing several crack elements within one specimen, the average and local maximum bond stresses were observed to be higher in longer crack elements. With large crack spacings, the concrete tensile stresses were also high, which appeared to favour splitting. This disproves the paradigm that elements experiencing splitting have lower local peak bond stresses than unconfined elements that do not split. On the contrary, the experimental results suggest the opposite, i.e. that splitting is caused by high bond stresses in combination with large crack spacing and concrete tensile stresses, with splitting causing lower bond stresses only in the post-peak phase. However, local bond stresses alone could not consistently explain the occurrence of splitting: Specimens with larger bar diameters were more prone to splitting despite the fact that bond stresses were observed to decrease with increasing bar diameter. However, the range of concrete tensile stresses – or the bond stresses multiplied by the bar circumference – were very similar in most specimens regardless of the reinforcing bar diameter. To conclude, high concrete tensile stresses combined with large crack spacings appeared to trigger splitting.

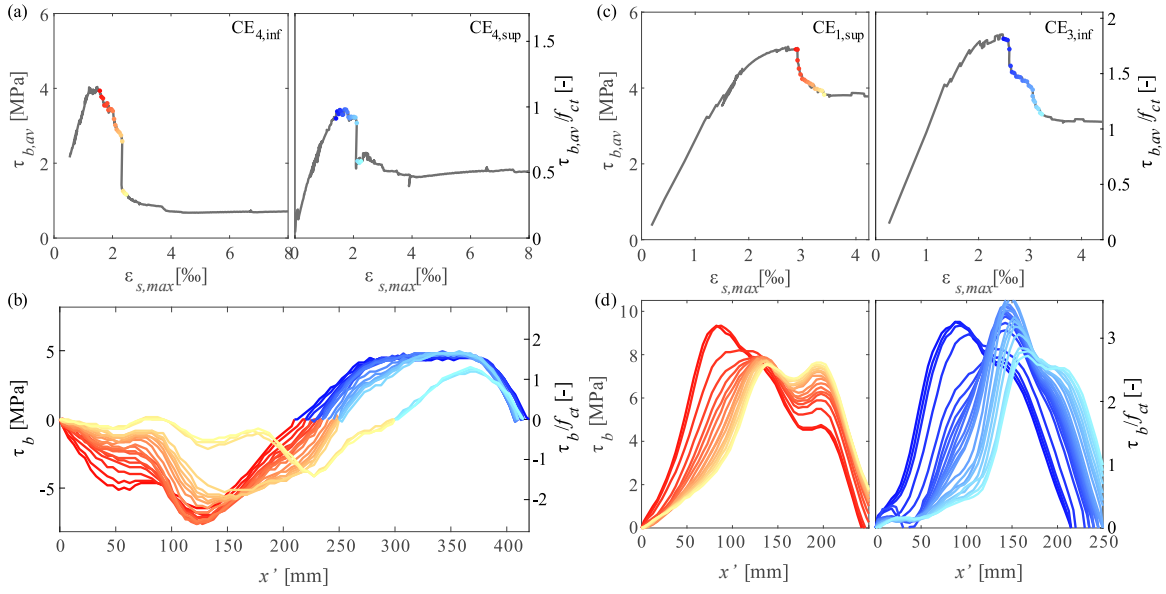

Fig. 26. Splitting of $CE_{4,inf}$ (red) and $CE_{4,sup}$ (blue) of Specimen Ø20.M.ND#1 and $CE_{1,sup}$ (red) and $CE_{3,inf}$ (blue) of Specimen Ø14.U.ND#3: (a), (c) average bond stresses against the steel strains at the crack and (b), (d) bond stress distribution over the parts of the CE before and after splitting. (For interpretation of the references to colour in this figure legend, the reader is referred to the web version of this article.)

The steel stiffness appeared to influence bond and the cracking behaviour as well. The bond stress distribution in a specimen reinforced with a bar exhibiting nonlinear elastic deformations already at low stresses (HD, Top12) was more uniform, with a larger crack spacing compared to specimens reinforced with conventional bars (with nonlinear deformations only close to yielding) in an otherwise identical specimen. In the latter, local bond stress peaks were much higher, while the crack spacing and concrete tensile stresses were lower. Conclusively explaining this behaviour is not straightforward and requires further research.

In the cyclic tests, slip reversal and unloading were observed immediately upon unloading over almost the entire length rather than gradually progressing from the cracks. After complete unloading in the elastic steel range, residual tensile stresses were observed in the steel bar at the cracks and a residual crack width remained. Unloading and reloading cycles had a detrimental effect on the bond stresses even when the cycles took place in the uncracked or crack formation stage. The deterioration did not become more severe after a small number of cycles (eight in the investigated specimen). Local bond stresses decreased due to unloading and reloading in the elastic range, while the slip was almost unaffected. Previously applied plastic deformations also had a deteriorating effect on bond.

The relative rib area was confirmed to be an important factor for crack control, which is largely neglected in current design codes (relying merely on a minimum value of this parameter). The higher the relative rib area was, the smaller the crack spacing, which could be related to higher initial bond stresses. However, the initial bond enhancement also favoured splitting and hence, crack widths were in a similar range regardless of the relative rib area. This indicates that providing sufficient confinement is essential to exploit the potential of reinforcing bars with high relative rib areas to reduce crack widths.

The measured bond stresses were significantly lower than typical values specified by design codes, which were typically calibrated based on pull-out tests. This difference can be explained by the intrinsically different conditions between a pull-out test and a tension tie. In a pull-out test, the embedment length is much shorter and the stresses are transferred from the bar through the surrounding concrete to a bearing plate by compression (axial components) and potentially partly by friction at the bearing plate-concrete interface (radial bursting stresses that are not carried by the concrete). Whereas in RC ties, bond stresses activate concrete in axial tension and potentially, a higher concrete confinement is mobilised. While this explains the lower observed bond stresses, it must be noted that the specimens did not have any transverse reinforcement, which is almost always present in practical applications, providing at least partial confinement and enhancing bond. Further experiments on structural elements with transverse reinforcement are required to validate the typical design values of bond used in serviceability verifications and quantify the effects of splitting and confinement.

CRediT authorship contribution statement

Tena Galkovski: Conceptualization, Validation, Investigation, Data curation, Writing – original draft, Visualization, Supervision, Project administration, Software, Formal analysis. **Jaime Mata-Falcón:** Conceptualization, Writing – review & editing, Supervision. **Walter Kaufmann:** Writing – review & editing, Supervision, Funding acquisition.

Declaration of Competing Interest

The authors declare that they have no known competing financial interests or personal relationships that could have appeared to influence the work reported in this paper.

Data availability

Some or all data, models, or codes that support the findings of this study are available from the corresponding author upon justified request.

Acknowledgements

The authors gratefully acknowledge the support by the staff of the structures laboratory at ETH Zurich (Bauhalle) during the preparation and testing of the experiments, Severin Haefliger, Andreas Näsbom, and Minu Lee from IBK Zürich for assisting with the DIC and DFOS strain measurement systems, Larissa Salis and Dominique Karlen for their support in the lab within the scope of their Master's theses, Alexander Beck and Andreas Näsbom from IBK Zürich for the co-supervision of Series 2, and Severin Haefliger for implementing the low pass filter in the fibre evaluation tool used in this study.

Appendix

A. Loading history for cyclic testing

The cyclic testing comprised one to three sets of cycles with constant lower and upper bound of the applied load F_{inf} and F_{sup} (see Table 1). Such typical loading histories are exemplarily shown for Specimens Ø14.U.ND#3 and Ø20.U.ND#1 in Fig. 22a and b.

B. Constitutive modelling of high-strength steel

The stress–strain relationship of the high-strength deformed reinforcing bars (grey lines in Fig. 23) was nonlinear already at low stresses, which cannot be captured by the Ramberg-Osgood [39] relationship (Fig. 23a, blue). Therefore, an eighth-order polynomial was fitted to the test data (six direct steel tests) and used for constitutive modelling (Fig. 23b).

C. Average bond stresses

To complement the results provided in the main part of the paper, average bond stresses of one additional specimen of each configuration are presented in Fig. 24.

It can be observed that the bond stresses of Specimen Ø14.M.ND#1 were unexpectedly low. While this could have been caused by the number of cracks (this specimen had three cracks and shorter crack elements), a closer examination reveals two further issues, which can be observed in Fig. 25 illustrating (a) the steel stresses and (b) the bond stresses obtained using both fibres FOa and FOb as well as the mean values, including a comparison to the theoretical stress at the cracks (applied load divided by the steel area). The results indicate that (i) the specimen was subjected to significant bending action (due to eccentricities), and (ii) since the average stresses at the crack do not correspond to the theoretical value, the reinforcing bar presumably was from a separate batch, having a different constitutive law than those of the material tests. The results of Ø14.M.ND#1 should therefore be discarded.

D. Extended analysis on the occurrence of splitting

Additional results about the occurrence of splitting influenced by the bar diameter are presented in this Annex. Fig. 26 shows the influence of splitting on the mean and local bond stress of specimens Ø20.M.ND#1 ($CE_{4,inf}$ and $CE_{4,sup}$) and Ø14.U.ND#3 ($CE_{1,sup}$ and $CE_{3,inf}$). $CE_{4,inf}$ and $CE_{4,sup}$ were located between two neighbouring cracks. $CE_{4,inf}$ had higher average bond stresses than $CE_{4,sup}$ prior to splitting (Fig. 26a). Due to splitting, average bond stresses decreased about 75% in $CE_{4,inf}$,

first progressively and then abruptly, presumably when the crack reached the surface (through-crack), as the bond stress distribution in Fig. 26b suggests. $CE_{4,sup}$ did not split. However, its transfer length decreased due to the splitting of $CE_{4,inf}$. This caused average stresses and local bond stresses to decrease also in $CE_{4,sup}$. Fig. 26c and d show the average and local bond stresses of $CE_{1,sup}$ and $CE_{3,inf}$ of Ø14.U.ND#3. As splitting started, bond stresses close to the crack decreased while they increased further away. Bond stresses were larger for the Ø14 mm bar, before and after splitting, compared to the Ø20 mm bar.

References

[1] Cairns J, Balázs GL, Cairns J, Eligehausen R, Lettow S, Metelli G, et al. fib Bulletin 72. Bond and anchorage of embedded reinforcement. Background to the fib Model Code for Concrete Structures 2010. fib. The International Federation for Structural Concrete. 2014.

[2] RILEM TC. RC 6 Bond test for reinforcement steel. 2. Pull-out test, 1983. RILEM Recommendations for the Testing and Use of Constructions Materials, London: E & FN Spon; 1994, p. 218–20.

[3] Lemcherreq Y. Strain-based analysis of reinforced concrete pull-out tests under monotonic and repeated loading. Eng Struct; 2022, submitted for review.

[4] Moreno DM, Trono W, Jen G, Ostertag C, Billington SL. Tension stiffening in reinforced high performance fiber reinforced cement-based composites. Cem Concr Compos 2014;50:36–46. https://doi.org/10.1016/j.cemconcomp.2014.03.004.

[5] Lagier F, Massicotte B, Charron J-P. Experimental investigation of bond stress distribution and bond strength in unconfined UHPFRC lap splices under direct tension. Cem Concr Compos 2016;74:26–38. https://doi.org/10.1016/j.cemconcomp.2016.08.004.

[6] Mains RM. Measurement of the distribution of tensile and bond stresses along reinforcing bars. J Proc 1951;48:225–52.

[7] Bresler B, Bertero V. Behavior of reinforced concrete under repeated load. J Struct Div 1968;94:1567–92. https://doi.org/10.1061/JSDEAG.0001981.

[8] Galkovski T, Lemcherreq Y, Mata-Falcón J, Kaufmann W. Fundamental studies on the use of distributed fibre optical sensing on concrete and reinforcing bars. Sensors 2021;21:7643. https://doi.org/10.3390/s21227643.

[9] Lemcherreq Y, Galkovski T, Mata-Falcón J, Kaufmann W. Application of distributed fibre optical sensing in reinforced concrete elements subjected to monotonic and cyclic loading. Sensors 2022;22:2023. https://doi.org/10.3390/s22052023.

[10] Kenel A, Marti P. Faseroptische Dehnungsmessungen an einbetonierten Bewehrungsstäben. vol. 271. Zürich, Switzerland: vdf Hochschulverlag, ETH Zürich; 2002.

[11] Kenel A. Biegetragverhalten und Mindestbewehrung von Stahlbetonbauteilen. Doctoral dissertation. Institut für Baustatik und Konstruktion. ETH Zürich 2002. https://doi.org/10.3929/ethz-a-004488185.

[12] Haefliger S, Mata-Falcón J, Kaufmann W. Application of distributed optical measurements to structural concrete experiments. SMAR 2017 Proceedings, ETH Zurich 2017.

[13] Fischer O, Thoma S, Crepaz S. Distributed fiber optic sensing for crack detection in concrete structures. Civil Eng Des 2019;1:97–105. https://doi.org/10.1002/cend.201900008.

[14] Cantone R, Fernández Ruiz M, Muttoni A. A detailed view on the rebar–to–concrete interaction based on refined measurement techniques. Eng Struct 2021;226:111332. https://doi.org/10.1016/j.engstruct.2020.111332.

[15] Brault A, Hoult N. Distributed reinforcement strains: measurement and application. ACI Struct J 2019;116. https://doi.org/10.14359/51714483.

[16] Mata-Falcón J, Haefliger S, Lee M, Galkovski T, Gehri N. Combined application of distributed fibre optical and digital image correlation measurements to structural concrete experiments. Eng Struct 2020;225:111309. https://doi.org/10.1016/j.engstruct.2020.111309.

[17] International Federation for Structural Concrete, editor. fib Bulletin 10. Bond of reinforcement in concrete: state-of-art report. Lausanne: International Federation for Structural Concrete; 2000.

[18] Kuuskoski V. Über die Haftung zwischen Beton und Stahl. Doctoral Thesis. The State Institute for Technical Research; 1950.

[19] Rehm G. Über die Grundlagen des Verbundes zwischen Stahl und Beton 1961;vol. Heft 138:p. 59.

[20] Lutz LA, Gergely P. Mechanics of bond and slip of deformed bars in concrete. JP 1967;64:711–21. https://doi.org/10.14359/7600.

[21] Hamad BS. Comparative bond strength of coated and uncoated bars with different rib geometries. MJ 1995;92:579–90. https://doi.org/10.14359/9776.

[22] Abrams DA. Tests of bond between concrete and steel. University of Illinois at Urbana Champaign, College of Engineering Engineering Experiment Station; 1913. Bulletin no. 71.

[23] Darwin D, Graham EK. Effect of deformation height and spacing on bond strength of reinforcing bars. ACI Struct J 1993;90:646–57.

[24] Hamad BS. Bond strength improvement of reinforcing bars with specially designed rib geometries. SJ 1995;92:3–13. https://doi.org/10.14359/1464.

[25] Metelli G, Plizzari GA. Influence of the relative rib area on bond behaviour. Mag Concr Res 2014;66:277–94. https://doi.org/10.1680/macr.13.00198.

[26] Tepfers R. Cracking of concrete cover along anchored deformed reinforcing bars. Mag Concr Res 1979;31:3–12. https://doi.org/10.1680/macr.1979.31.106.3.

[27] Goto Y. Cracks formed in concrete around deformed tension bars. JP 1971;68:244–51. https://doi.org/10.14359/11325.

[28] Gambarova PG, Rosati G. Bond and splitting in reinforced concrete: test results on bar pull-out. Mater Struct 1996;29:267–76. https://doi.org/10.1007/BF02486361.

[29] Marti P, Alvarez M, Kaufmann W, Sigrist V. Tension chord model for structural concrete. Struct Eng Int 1998;8:287–98. https://doi.org/10.2749/101686698780488875.

[30] SIA. Swisscode SIA 262: Concrete Structures. Zurich, Switzerland: Swiss Society of Engineers and Architects (SIA); 2013.

[31] EN 1992-1-1. Eurocode 2: Design of concrete structures - Part 1-1 : General rules and rules for buildings 2004.

[32] International Federation for Structural Concrete. fib model code for concrete structures 2010. Berlin: Ernst & Sohn; 2013.

[33] Chen WF. Double punch test for tensile strength of concrete. ACI J 1970;67:993–5.

[34] Correlated Solutions. Vic-3D Software Manual; 2019.

[35] Gehri N, Mata-Falcón J, Kaufmann W. Automated crack detection and measurement based on digital image correlation. Constr Build Mater 2020;256:119383. https://doi.org/10.1016/j.conbuildmat.2020.119383.

[36] Gehri N, Mata-Falcón J, Kaufmann W. Refined extraction of crack characteristics in Large-scale concrete experiments based on digital image correlation. Eng Struct 2022;251:113486. https://doi.org/10.1016/j.engstruct.2021.113486.

[37] LUNA Inc. Users Guide ODiSI-A Software 1.3; 2013.

[38] LUNA ODiSI 6000 Data Sheet; 2021.

[39] Ramberg W, Osgood WR. Description of stress-strain curves by three parameters. n. d.

[40] Kaufmann W, Galkovski T. Spannungszustand in ungerissenen Betonbauten. Zurich: Institute of Structural Engineering, ETH Zurich; 2019.

[41] Koppitz R, Kenel A, Keller T. Tension chord model modification for uniaxial unloading and reloading in elastic and plastic states. J Struct Eng 2014;140:04014077. https://doi.org/10.1061/(ASCE)ST.1943-541X.0000999.

[42] Passos Sério Lourenço MF, Fernández Ruiz M, Haugerud SA, Blaauwendraad J, Bousias S, Hoang LC, et al. fib Bulletin 100. Design and assessment with strut-and-tie models and stress fields: from simple calculations to detailed numerical analysis. fib. The International Federation for Structural Concrete. 2021.

[43] Hordijk DA. Tensile and tensile fatigue behaviour of concrete; experiments, Modelling and Analyses'. Heron 1992;37:1–79.

[44] Muttoni A, Fernández RM. Concrete cracking in tension members and application to deck slabs of bridges. J Bridg Eng 2007;12:646–53. https://doi.org/10.1061/(ASCE)1084-0702(2007)12:5(646).

[45] Lemcherreq Y, Zanuy C, Vogel T, Kaufmann W. Experimental and analytical assessment of fatigue damage in reinforced concrete tension members. Engineering Structures n.d.;sumbitted for review; November 2022.